# Predicting the efficacy of BH3 mimetics through the profiling of multiple protein complexes in acute myeloid leukemia

Changju Chun[1,5], Ja Min Byun[2,5], Minkwon Cha[1,4,5], Hongwon Lee[3], Byungsan Choi[3], Hyunwoo Kim[3], Saem Hong[3], Yunseo Lee[3], Hayoung Park[3], Youngil Koh[2*], and Tae-Young Yoon[1,3*]

[1]School of Biological Sciences and Institute for Molecular Biology and Genetics, Seoul National University, Seoul 08826, South Korea

[2]Department of Internal Medicine, Seoul National University College of Medicine, Seoul National University Hospital 03080, Seoul, South Korea

[3]Department of Biomarker Discovery, PROTEINA Co., Ltd, Seoul 08826, South Korea

[4]Present address: Department of Physics, Pohang University of Science and Technology (POSTECH), Pohang 37673, South Korea

[5]These authors contributed equally

*Corresponding authors, go01@snu.ac.kr; tyyoon@snu.ac.kr

**Abstract**

**BH3 mimetics are protein-protein interaction (PPI) inhibitors that saturate anti-apoptotic proteins in the BCL2 family to induce apoptosis in cancer cells, a prominent example of protein complex-targeting therapies. Despite the remarkable success of the BH3 mimetic ABT-199 in treating hematological malignancies, only a fraction of patients respond to ABT-199 and eventually develop resistance, necessitating the predictive biomarkers for both initial responses and resistance development. We here used the single-molecule pull-down and co-immunoprecipitation platform to quantify more than 20 different types of PPI complexes using ~1.2x10$^6$ cells in total, revealing the rewired status of the BCL2 family PPI network. By comparing the obtained multi-dimensional data with BH3 mimetic efficacies determined *ex vivo*, we constructed an analysis model for ABT-199 efficacy that designates the BCL2-BAX and BCLxL-BAK complexes as the primary mediators of drug effectiveness and resistance. We then applied this model to assist in therapeutic decision-making for acute myeloid leukemia patients in a prospective manner. Our work demonstrates a capability for the extensive characterization of PPI complexes in clinical specimens, potentially opening a new avenue of precision medicine for protein complex-targeting therapies.**

Cells employ large protein complexes to make intricate decisions, reflecting diverse cellular states[1,2]. Prominent examples include regulation by mammalian target of rapamycin (mTOR) complexes in metabolism[3], inflammasomes in innate immunity[4] and BCL2 family complexes in apoptotic cell death[5]. Despite the unexpected breadth of associated proteins and their rapid turnover in these complexes, connectivity amongst several core components still defines critical setpoints in cellular decision-making. For example, across possible combinations of the BCL2 family proteins, the formation of proteinaceous pores by BAX and BAK leads to mitochondria outer membrane permeabilization (MOMP), making a point of no return for apoptosis initiation[6-8]. The survival and apoptotic pressure accrued in cells are reflected by the expression of anti- and pro-apoptotic proteins, tipping the scale toward survival or apoptosis, respectively. While BCL2, BCLxL, and MCL1 make up the group of anti-apoptotic proteins that sequester BAX/BAK to prevent pore formation[5,9-11], pro-apoptotic proteins (such as BIM, BAD, and BID) share an alpha-helical BH3-domain and interact with either anti-apoptotic proteins or BAX/BAK[12-14], thereby unleashing the activation of BAX/BAK for pore formation[15,16].

In diseased states, cellular decisions are often misguided by chronic or spurious formation of these protein complexes, as seen with mTOR complexes found in various cancers or type 2 diabetes[17,18] and inflammasomes in irritable bowel syndrome or neurodegenerative diseases[19,20]. Likewise, many cancers exhibit upregulated PPIs of the anti-apoptotic proteins to suppress the activity of BAX/BAK, thus averting apoptosis initiation[10,16,21-23]. Consequently, extensive efforts have been made to develop PPI inhibitors that can disintegrate disease-causing protein complexes[24]. In particular, BH3 mimetics, small-molecule drugs that structurally emulate the BH3 domain, are a notable example in these endeavors[25,26]. While sparing pro-apoptotic proteins, BH3 mimetics are expected to bind selectively to the binding grooves of the anti-apoptotic proteins to shut down their interactions with pro-apoptotic proteins and BAX/BAK[27]. By introducing an azaindole moiety to ABT-263 (Navitoclax) that binds to both BCL2 and BCLxL[28], ABT-199 (Venetoclax) has been developed to specifically bind to BCL2 with a sub-nM affinity[29]. ABT-199 was approved for the treatment of chronic lymphoid leukemia (CLL) in 2016 (NCT01889186)[30] and acute myeloid leukemia (AML) in 2018 (NCT02287233, NCT02203773)[31,32], which stimulated the development of other BH3 mimetics that target other anti-apoptotic proteins beyond BCL2[27,33].

In line with other targeted therapies, a precision medicine platform could facilitate the customized use of PPI inhibitors, using the unique molecular information of individual patients[34]. Despite ABT-199's remarkable success in treating CLL[35,36], over 30% of AML patients still fail to respond[32,37,38], and many with initial favorable responses eventually develop resistance[39,40]. These facts underscore unmet needs where diverse treatment options could benefit patients if initial responses or resistance development could be accurately predicted. However, multiple factors, including post-translational modifications, protein conformational changes, and cellular localizations, may hinder the direct translation of genomic and proteomic information into accurate PPI strength predictions[5,41,42]. Genomic and proteomic profiling have thus found limited use in this technical niche[43-45], and correlations between total expression levels of BCL2 and other anti-apoptotic proteins and response to BH3 mimetics have not been robust enough for clinical application[46-49]. While the BH3 profiling method offers potential usefulness in predicting BH3 mimetics, it is not routinely used in clinical settings, likely due to the need for sample viability maintenance[50-52].

In this work, we hypothesize that the responsiveness of individual cancers to a PPI inhibitor would be determined by the ever-evolving compositions of the target protein complexes. Specifically, in the case of

77 BH3 mimetics, the heterocomplexes between anti- and pro-apoptotic proteins and their intricate balances
78 may primarily mediate the efficacy of BH3 mimetics in given cancers. We propose that a predictive algorithm
79 may be trained by extensively profiling BCL2 family protein complexes in as many cancers with known
80 responses as possible. To enable such profiling with minimal sample consumption and increased
81 throughput, we adopted the single-molecule pull-down and co-immunoprecipitation (SMPC) platform, directly
82 immobilizing target protein complexes on the imaging plane of a single-molecule fluorescence microscope
83 and counting the number of complexes[53-56]. This approach allowed us to determine the populations of 20
84 different types of protein complexes (and protein levels) using only ~30,000 cells per complex type, revealing
85 the latest rewiring status of the BCL2 family network in individual clinical samples.

86 We found that the introduction of bacterial toxin and BH3 mimetics caused significant changes in the
87 composition of BCL2 protein complexes, with only minor alterations in corresponding protein levels. This
88 finding underscores the importance of directly profiling protein complexes rather than merely analyzing
89 protein levels. By correlating these multi-dimensional data with the *ex vivo* determined efficacies of BH3
90 mimetics, we were able to train analytical models that identified the protein and PPI parameters playing
91 pivotal roles in mediating the efficacy of BH3 mimetics. For ABT-199, we found that the counts of two specific
92 complexes, BCL2-BAX and BCLxL-BAK, served as critical contrasting analysis parameters, with the former
93 driving ABT-199's efficacy and the latter contributing to resistance development. Following a similar
94 procedure, we constructed an efficacy model for an MCL1-targeting inhibitor. Subsequently, we applied the
95 developed analytical model to guide therapeutic decisions for AML patients in a prospective fashion,
96 confirming the model's predictive power. Our work showcases the utility of the SMPC platform for extensive
97 and accurate profiling of protein complexes and presents a path toward precision medicine in therapies
98 targeting protein complexes.

99

100 ## Results

101 ### Profiling BCL2 family protein complexes using SMPC

102 To assess BCL2 family protein complexes and gain insights into how apoptosis is suppressed in individual
103 cancers, we utilized the SMPC platform to characterize the PPI network among BCL2 family proteins[53,54,56,57].
104 We initiated surface immunoprecipitation (IP) of one of the primary anti-apoptotic proteins (i.e., BCL2,
105 BCLxL, or MCL1) from crude cell extracts (Fig. 1a and Extended Data Fig. 1a-c), followed by the addition of
106 a monoclonal antibody that binds to the interaction partner complexed with the surface-immobilized bait. A
107 fluorescently labeled secondary antibody was then used, completing an immunoassay to detect specific
108 protein complexes (CPXs) (Fig. 1b, left). Additionally, we employed a detection antibody that binds to an
109 epitope directly on the surface bait to determine the total amount of surface-immobilized baits (protein total
110 level, LV) (Fig. 1b, right and Extended Data Fig. 1d-f).

111 To enhance sensitivity and reproducibility in this protein complex detection method, we optimized the
112 lysis protocol[57,58]. By using HEK293T cells co-expressing BCL2 and the BH3 domain of BIM ($BIM_{BH3}$), we
113 found that mild lysis with cholesterol-like detergents, such as glycol-diosgenin (GDN) and digitonin,
114 minimized dissociation of the model BCL2-BIM complexes (Extended Data Fig. 1g). Furthermore, this lysis
115 protocol did not induce the formation of spurious complexes even in dense cell extracts (i.e., at a total protein

116 concentration of 5 to 10 mg/ml), confirming that all detected protein complexes were formed in cellular
117 environments (Fig. 1c). Conformational changes of the BCL2 family proteins during their activation are
118 crucial in their function[16,59]. For instance, the pore formers, BAX and BAK, expose their α1 helices in the
119 activated state, which are otherwise buried in the core structure. By assessing the active status of BAX using
120 an anti-α1 helix antibody, we found that the detergent condition significantly affected BAX's conformational
121 state[2,60]. Triton X-100, often used in conventional co-IP methods, induced spurious conformational
122 changes[61], while GDN essentially preserved BAX's active conformations induced by the addition of a
123 bacterial toxin, staurosporine (STS)[62] (Fig. 1d). Similarly, we experimentally confirmed the ability to assess
124 the activation status of BAK[63,64], by employing an antibody that specifically binds to the α1 helix of BAK
125 (Extended Data Fig. 1h,i). Finally, we experimentally confirmed that a single freeze-thaw cycle did not
126 seriously affect the single-molecule counts of BCL2 protein complexes (Extended Data Fig. 1j-l).

127 To minimize non-specific adsorption to the surface, we placed a high-density polyethylene glycol
128 (PEG) layer between the IP antibodies and the glass coverslip[57,58] (Fig. 1a). This PEG layer proved essential
129 in enabling direct surface IP of the target protein complexes from the crude extracts reducing background
130 signals to a minimal level on our single-molecule fluorescence imaging (Fig. 1e). By effectively removing
131 background signals through signal processing, we could identify single-molecule fluorescence spots and
132 directly count their numbers (Extended Data Fig. 2a-c)[55,65]. Compared with conventional approaches that
133 integrate total fluorescence signals over a field of view, this single-molecule counting method maintained
134 signal-to-noise ratios higher than 5 when there were ~1,000 or fewer individual single-molecule spots per
135 imaging area (Fig. 1f and Extended Data Fig. 2).

136 Through the combination of the three technological factors of optimized lysis protocol, anti-fouling PEG
137 layer, and direct single-molecule counting, we achieved statistically significant counts for endogenous BCL2-
138 BIM or BCL2-BAX CPXs using only ~30,000 AML cells (Fig. 1g,h). We also demonstrated a similar capability
139 using a non-small cell lung cancer cell line (PC9 cells), where we detected 8 different BCLxL- and MCL1-
140 protein complexes using less than 50,000 PC9 cells each (Fig. 1i and Extended Data Fig. 3). Three
141 independent inter-chip measurements yielded coefficients of variation (CVs) of less than 15% for all assays
142 and cell numbers tested, confirming the high stability of the established SMPC platform (Fig. 1h,i and
143 Extended Data Fig. 3).

144

145 **Tracking the responses to apoptotic stress using SMPC**

146 To investigate if the developed SMPC platform could monitor alterations within the BCL2 family PPI network,
147 HL60 cells were treated with 2 μM of STS. The crude extracts were obtained from these cells at various time
148 points during the treatment (Extended Data Fig. 4a). Through flow cytometry analysis, the early apoptosis
149 population, characterized by high Annexin V staining, was observed to surge at 1 hour of STS treatment,
150 reducing the healthy cell population (Extended Data Fig. 4a,b). The late apoptosis population, stained with
151 both Annexin V and PI, increased after 4 hours. Necrosis populations remained negative throughout the
152 study, signifying that the cells underwent apoptosis rather than necrosis.

153 We observed that the counts of active BAX and BAK dramatically increased as apoptosis progressed
154 (Fig. 2a). The count of BAX-BAK heterocomplexes, a more direct surrogate marker of MOMP[66,67], began to

155 rise simultaneously with the active BAX and BAK counts, but continued to escalate into the late apoptosis
156 stage. We then quantified the total levels of anti-apoptotic proteins (Fig. 2b). Through careful calibration of
157 immunolabeling efficiencies (Extended Data Fig. 5a-c), we were able to directly compare the quantities of the
158 primary anti-apoptotic proteins and their protein complexes (Fig. 2b-d). We found that BCL2 proteins were
159 more abundant by 4 to 5 times compared to BCLxL and MCL1, aligning with the known dependence of HL60
160 on BCL2 (Fig. 2b). As apoptosis progressed, BCLxL and MCL1 levels gradually diminished, while BCL2
161 protein levels exhibited a slight yet significant increase.

162 Contrary to the minimal change in BCL2 protein level, the heterocomplexes formed between BCL2
163 and pro-apoptotic proteins displayed dynamic changes throughout the apoptosis stages. We discovered that
164 BCL2 protein complexes outnumbered those involving BCLxL and MCL1, further confirming HL60's BCL2-
165 dependence (Fig. 2c,d). Notably, the two protein complexes exhibited contrasting behaviours. While the
166 counts of the BCL2-BIM complex gradually decreased over time, the BCL2-BAX complex counts surged for
167 the first 2 hours following STS treatment (Fig. 2c,d). Collectively, our comprehensive profiling of the BCL2
168 family protein complexes revealed that BCL2 proteins mainly functioned to sequester the active BAX
169 proteins during STS-induced apoptotic pressure in HL60, while simultaneously releasing some previously
170 held BIM proteins. Presumably, under the applied STS treatment conditions, the active BAX outnumbered
171 the BCL2's sequestration capacity, leading to the HL60 cells succumbing to apoptotic stress and initiating
172 MOMP (Fig. 2a,d).

173

174 **Assessment of potential PPIs using protein interactor probes**

175 Our findings reinforce the understanding that BCL2 family proteins, akin to many cell signalling proteins,
176 function by binding to (or sequestering) interaction partners[4]. During elevated survival pressure in HL60 cells
177 induced by STS treatment, the BCL2 proteins consistently formed additional BCL2-BAX complexes to
178 counteract apoptotic pressure (Fig. 2d). This led us to conceive additional assays to evaluate the capacity of
179 BCL2 family proteins to form further protein complexes beyond current complex populations.

180 To evaluate the affinities of potential PPIs, we employed the same surface pull-down approach to
181 immobilize anti-apoptotic BCL2 family proteins, a procedure confirmed to cause minimal IP crosstalk and
182 non-specific adsorption (Fig. 2e). Various pro-apoptotic BCL2 proteins, tagged with enhanced green
183 fluorescent proteins (eGFPs), were then introduced into the reaction chamber. We hypothesized that these
184 PPI probes would engage with a pool of anti-apoptotic proteins that were unoccupied but still capable of
185 forming potential protein complexes (Fig. 2e). Indeed, this PPI probe binding assay not only allowed us to
186 replicate the dissociation constants for the binding interactions between the anti- and pro-apoptotic proteins,
187 but also faithfully reproduce known biochemical features (Extended Data Fig. 6a-h)[5,52]. These included a
188 higher affinity of BCL2 for BAD compared to BIM and negligible interactions for BCL2-NOXA and MCL1-BAD
189 pairs (Extended Data Fig. 6e,f)[4]. We further verified that these PPI probes did not disrupt the pre-existing,
190 endogenous protein complexes (Extended Data Fig. 6i).

191 Utilizing this probe binding assay (PBA), we analyzed BCL2 proteins extracted from the STS-treated
192 HL60 cells (Extended Data Fig. 4b). By employing the BH3 domain of BIM ($BIM_{BH3}$-eGFP) as a PPI probe,
193 BCL2 exhibited a significantly higher PBA count in comparison to BCLxL and MCL1 (Fig. 2f). Given the

194 higher affinities of the $BIM_{BH3}$ domain for BCLxL and MCL1 than for BCL2 (Extended Data Fig. 6b), this
195 elevated PBA count suggests that BCL2 works as a larger reservoir in sequestering pro-apoptotic proteins
196 compared to BCLxL or MCL1 in HL60 (Fig. 2f). Strikingly, as apoptosis progressed, the PBA count of $BIM_{BH3}$
197 declined, despite the rise in total BCL2 levels, possibly indicating the exhaustion of available BCL2 proteins
198 through the formation of BCL2-BAX complexes (Fig. 2c-f). Furthermore, we inspected the composition of the
199 BCL2 protein complexes in four AML cell lines (Fig. 2g). When immobilizing an equivalent number of total
200 BCL2 proteins per view (Fig. 2g, right), NB4 and U937 cells were found to contain substantially more BCL2-
201 BIM and BCL2-BAX complexes, the two main species of BCL2 protein complex species, compared to HL60
202 (Fig. 2h). This observation corresponded with the PBA count being more than halved for NB4 and U937
203 relative to HL60 (Fig. 2i), reflecting increased BCL2 occupancy and thereby reduced pools of BCL2 proteins
204 available for potential PPIs in these cells (Fig. 2j). It was noteworthy that the combined totals of the PBA and
205 protein complex counts accounted for 60 to 80% of the total BCL2 proteins in the cell lines we investigated.
206 This suggests that a significant proportion of BCL2 proteins may be complexed with interaction partners not
207 accounted for in our study (Fig. 2j).

208 Finally, we investigated whether different PPI probes target the same pool of BCL2 proteins or distinct,
209 separate BCL2 pools (i.e., each pool accessible by only specific PPI probes). To answer this question, we
210 introduced multiple PPI probes simultaneously and found that these probes directly competed with one
211 another, as well as with ABT-199 (Fig. 2k and Extended Data Fig. 6j,k). In addition, the consistency of the
212 PBA counts across different cell lines and PPI probes indicated the existence of a singular, common BCL2
213 protein pool, rather than multiple, fragmented pools of BCL2 proteins (compare Fig. 2i with Extended Data
214 Fig. 6l-n).

215

216 **Tracing changes in the BCL2 family protein complexes provoked by BH3 mimetics**

217 Leveraging the two assays we established (namely, single-molecule immunoassay and PBA), we set out to
218 explore how BH3 mimetics instigated apoptotic pressure in AMLs. We exposed HL60 cells to 100 nM ABT-
219 199 for 24 hours, resulting in a modest ~30% increase in the total BCL2 level, while BCLxL and MCL1 levels
220 remained minimal (Fig. 3a). Conversely, the amounts of active BAX and BAK, along with BAX-BAK
221 heterocomplexes, surged five-fold after ABT-199 treatment, signalling active apoptosis induction in HL60
222 (Fig. 3b). Although total BAX and BAK populations were largely consistent (Fig. 3c), the majority of the
223 BCL2-BIM and BCL2-BAX complexes dissociated due to ABT-199 exposure (Fig. 3d). These findings
224 highlight that BAX, once released from BCL2, mainly contributed to the steep increases in active BAX and
225 BAK populations. Additionally, ABT-199's liberation of BCL2 proteins led to an elevated PBA count – a direct
226 contrast to the STS-treated case where the PBA count dwindled over the treatment period (Fig. 3e).

227 To delineate the dynamics of BCL2-BIM and BCL2-BAX complexes, especially at early ABT-199
228 treatment stages, we administered a higher 300 nM concentration of ABT-199 to HL60 cells and conducted
229 PPI profiling at each hourly interval following initial treatment (Extended Data Fig. 4c). The two major BCL2
230 complexes showed opposing results. The BCL2-BAX complex began to unravel instantly after ABT-199
231 administration, while the number of BCL2-BIM complexes largely persisted (Fig. 3f). The kinetics of BCL2-
232 BAX dissociation synchronized with the activation of BAX/BAK conformations and BAX-BAK
233 heterocomplexes (Fig. 3g). This data suggested that the dissociation of BCL2-BAX complexes – without

234 necessitating BCL2-BIM dissociation or additional BAX expression – likely sufficed to invoke pro-apoptotic
235 pressure and initiate apoptosis (Fig. 3f-i)[43,68-70].

236 We further investigated whether similar complex dynamics were observable in MCL1 inhibitor-
237 responsive cells. In reaction to AZD-5591[71], U937 cells exhibited augmented populations of active BAX and
238 BAK proteins, along with BAX-BAK heterocomplexes, consistent with U937's susceptibility to the MCL1
239 inhibitor (Fig. 3j). Mirroring the case with ABT-199-treated HL60 cells, AZD-5591 treatment spurred a
240 conspicuous dissociation of MCL1 protein complexes (MCL1-BIM and MCL1-BAK), evidenced by the
241 pronounced increase in $BIM_{BH3}$ probe binding for MCL1 (Fig. 3k,l). However, unlike the HL60 case where
242 other anti-apoptotic proteins demonstrated minimal alterations, BCLxL proteins in U937 cells exhibited
243 significant surges in their complex counts, with BCLxL-BAK complexes becoming preeminent (Fig. 3m). A
244 thorough calibration of labeling efficiencies allowed us to discern that the observed rise in BCLxL-BAK
245 markedly outpaced the decrease in MCL1-BAK complexes (Fig. 3n and Extended Data Fig. 5a,c). We
246 consequently hypothesized that the majority of new BCLxL-BAK complexes originated from the sequestering
247 of nascent BAK proteins, rather than capture from those liberated from MCL1 (Fig. 3o). In summation, these
248 data substantiate the feasibility of comprehensive profiling of BCL2 family protein complexes, enhancing our
249 understanding of how apoptotic pressure is both generated and managed by the BCL2 family protein
250 network within individual cancers.

251

252 **Constructing an analysis model for ABT-199 efficacy with multi-dimensional PPI profiling.**

253 So far, our collective data suggest that BH3 mimetics work through either protein complex disintegration,
254 saturation of anti-apoptotic proteins, or both to achieve their effects. Additionally, preliminary findings hint at
255 a single-agent response when cancer cells show a specific dependence on a singular anti-apoptotic protein,
256 with minimal compensation from other anti-apoptotic proteins (Extended Data Fig. 7). We therefore decided
257 to investigate whether multi-parameter data could be used to develop an analytical model to identify the
258 dependency on anti-apoptotic proteins for specific cancers and forecast their responsiveness to BH3 mimetic
259 drugs.

260 For this purpose, we analyzed 32 primary AML samples, of which 30 were gathered from bone marrow
261 mononuclear cells (BMMCs) and 2 from peripheral blood mononuclear cells (PBMCs) (Fig. 4a). The clinical
262 diagnoses included *de novo* AML (*n*=17), relapsed AML (*n*=4), and secondary AML (*n*=11) (Supplementary
263 Table 1). We evaluated the *ex vivo* effectiveness of ABT-199, determining a normalized area under the
264 response curve (AUC) for each specimen (Fig. 4a, upper). Concurrently, the SMPC PPI profiling was
265 performed on the same cohort samples in a blind fashion, allowing the determination of 22 unique
266 protein/PPI metrics for each sample comprised of roughly $1.2 \times 10^6$ cells in total (Fig. 4a, lower and
267 Supplementary Table 2).

268 Upon comparing the protein/PPI assay data with AUC, four BCL2-related metrics – BCL2-BAD PBA,
269 BCL2-$BIM_{BH3}$ PBA, BCL2-BAX CPX and BCL2 total level – exhibited the highest correlations with *ex vivo*
270 efficacy (Fig. 4b). Although BCLxL- and MCL1-related metrics also showed appreciable correlations, the
271 correlation values were lower, signaling that most AML cases examined relied on BCL2 for survival (Fig. 4b).
272 Interestingly, the BCL2-BIM complex showed a much lower correlation than the BCL2-BAX complex count,
273 reflecting our observation that the BCL2-BAX complexes' dissociation predominantly mediated the pro-

274 apoptotic effects of ABT-199 in HL60 cells (Fig. 4b-d). A simple combination of the four BCL2-related metrics
275 only led to limited improvements in correlation while losing statistical significance, possibly due to redundant
276 information concerning the BCL2 protein pool's molecular status (Extended Data Fig. 8a,b and see below).

277 To explore metric combinations in a broader parametric space, we divided the 32 AML samples into
278 responsive and non-responsive groups using an *ex vivo* AUC threshold of 0.61, corresponding to an $IC_{50}$ of
279 100 nM ABT-199 (Extended Data Fig. 8c)[72,73]. We then examined approximately 10,000 different models,
280 each with varying metric combinations and coefficients, selecting 67 models that made accurate predictions
281 for the training set responsiveness, as validated by the remaining test samples (Extended Data Fig. 8d).
282 Remarkably, the final 67 models consistently identified a subgroup of selected metrics rather than displaying
283 diverse metrics randomly (Fig. 4e). Two metrics, BCLxL-$BIM_{BH3}$ PBA and BCLxL-BAK CPXs, were negatively
284 correlated with *ex vivo* AUC values, presumably reflecting a compensatory role for BCLxL in counteracting
285 accumulated apoptotic pressure in AMLs.

286 Upon detailed examination of the 67 models, we noticed a pattern where the information from each
287 metric displayed minimal overlap. For example, while combining the BCL2-BAX CPX and BCL2-$BIM_{BH3}$ PBA
288 data successfully (which represented occupied and unoccupied portions of BCL2), neither metric could be
289 combined with the BCL2 total level data (which included both occupied and unoccupied pools), likely due to
290 partial overlap in the information they provided (Extended Data Fig. 8a). Similarly, the BCLxL-BAK CPX
291 consistently exhibited higher absolute values in its correlations to *ex vivo* AUC than BCLxL-BAX CPX,
292 possibly because of redundancy in the information concerning BAX that was already considered by the
293 inclusion of the BCL2-BAX CPX metric (Fig.4e). As a result, a combination of BCL2-$BIM_{BH3}$ PBA, BCL2-BAX
294 CPX, and BCLxL-BAK CPX (with a negative coefficient) was selected, showing a slight but significant
295 enhancement in the correlation to AUC values with statistical significance ($p$-value<0.05) for all metrics
296 examined (Fig. 4f). In the receiver operating characteristic (ROC) analysis for binary prediction (responsive
297 versus non-responsive), the resulting AUC showed the highest values for the combined model compared to
298 single-metric models (Fig. 4g,h). Moreover, the mean squared error (MSE) was determined to be the
299 smallest for the combined model, indicating higher accuracy in estimating ABT-199 efficacy (Fig. 4h).

300 We tested whether the created model could illustrate changes in the BCL2 PPI network as AML
301 underwent clonal cancer evolution. For instance, BC-7064, a primary AML case, initially responded favorably
302 to combined treatment with ABT-199 and azacitidine but relapsed after discontinuing the treatment (Fig. 4i).
303 We performed PPI profiling on the initial (BC-7064) and relapsed (BC-7064-R) samples using our platform in
304 a retrospective manner, comparing the three diagnostic PPI metrics in the combined model (Fig. 4i). The
305 initial sample exhibited parameters indicative of strong ABT-199 effectiveness (estimated score of 0.78),
306 composed of upregulated BCL2-$BIM_{BH3}$ PBA and BCL2-BAX CPX counts and a low BCLxL-BAK CPX level
307 (Fig. 4j). Conversely, the two BCL2-related metrics were more than halved for BC-7064-R, signaling a
308 reduced driving force for ABT-199 efficacy. Although the resistance factor BCLxL-BAK complex also
309 decreased for BC-7064-R, the weakened BCL2 dependence led to an estimated score of 0.36, explaining
310 the relapse of this specific blood cancer (Fig. 4i,j).

311 Finally, we sought to make quantitative comparisons between our BCL2 PPI profiling and other
312 established methods for predicting BH3-mimetic effectiveness, such as BH3 profiling[74,75]. BH3 profiling
313 involves the addition of BH3 peptides derived from BIM, BAD, and HRK to individual AML samples after cell

314 permeabilization, with mitochondrial depolarization monitored using JC-1 dye fluorescence (Extended Data
315 Fig. 9a, upper). In our study, HL60 cells demonstrated robust depolarization signals in response to the BAD
316 peptide, but not to the HRK peptide, a finding consistent with prior research (Extended Data Fig. 9b,c)[52,76].
317 We continued by examining 14 primary AML samples from the same cohort (due to limited sample
318 availability) and tested various combinations of the depolarization signals elicited by BIM, BAD, and HRK
319 peptides at different concentrations (Supplementary Table 3). We found that a combination that examined
320 the difference between BAD and HRK signals (both measured at 10 μM peptides) yielded the highest
321 correlation value of 0.65 with *ex vivo* ABT-199 efficacy (Extended Data Fig. 9d). Importantly, for this smaller
322 cohort consisting of 14 AML samples, the BCL2 PPI profiling essentially maintained the performance
323 parameters examined, including correlation, MSE, and AUC from the ROC analysis, which were superior to
324 those determined for the BH3 profiling (Extended Data Fig. 9d-g). Attempts to use the BCL2 level measured
325 by flow cytometry as a predictive marker (Extended Data Fig. 9a, lower) only resulted in muted performance
326 across all evaluated parameters, further emphasizing the effectiveness of our profiling technique in
327 estimating ABT-199 efficacy (Extended Data Fig. 9h-j).

328

329 **Construction of an MCL1 inhibitor efficacy model**

330 Next, we investigated the possibility of training an analysis model for the MCL1 inhibitor AZD-5991,
331 employing a similar process to that which we established for ABT-199. For this purpose, we evaluated the *ex*
332 *vivo* efficacy of AZD-5991 on the same primary AML cohort (27 out of 32 total samples), comparing the
333 determined AUC values with the BCL2 family metrics outlined in Figure 4 (Supplementary Table 2). Both the
334 total MCL1 level and the MCL1 PBA count displayed correlation with AZD-5991 efficacy, though the
335 correlations were diminished (Fig. 5a-c). Notably, the $BIM_{BH3}$ PBA assay for BCLxL exhibited a negative
336 correlation with AZD-5991 efficacy (Fig. 5d). Plotting the BCLxL PBA counts for responsive (*ex vivo*
337 AUC≥0.61) versus non-responsive samples concerning AZD-5991 revealed that the non-responsive group
338 manifested distinctly higher counts[72,73], indicative of upregulated activities of BCLxL proteins within this group
339 (Fig. 5e and Extended Data Fig. 8f). These collective findings suggest that BCLxL proteins play a substantial
340 compensatory role when MCL1 proteins are saturated with inhibitor molecules. Furthermore, MCL1 protein
341 complexes presented only limited correlations to *ex vivo* AUC, aligning with our hypothesis presented in
342 Figure 3 that AZD-5991 may operate by preventing additional binding of pro-apoptotic proteins to MCL1 (i.e.,
343 saturation of MCL1 proteins), rather than inducing dissociation of pre-existing MCL1 protein complexes (Fig.
344 5a).

345 Integrating multiple parameters, namely the MCL1 total level, BCLxL-$BIM_{BH3}$ PBA, and BCLxL-BAK
346 CPX, we formulated a linear regression model that yielded an optimized correlation with the *ex vivo* AZD-
347 5991 efficacy (Fig. 5f). While several BCL2-related parameters alone already displayed high correlations with
348 ABT-199 efficacy (signaling the singular dependence on BCL2) (Fig. 4b), the MCL1-related metrics required
349 combination with BCLxL-involving metrics to enhance the correlation, pointing to a complex interplay and
350 dynamic between MCL1 and BCLxL protein pools (Fig. 5a,f and Extended Data Fig. 8e). The principle of
351 minimal information overlap between metrics appeared to be preserved here as well, given that the final
352 combination encompassed occupied and unoccupied populations of both MCL1 and BCLxL with seemingly
353 minimal overlap. Through the combined model for AZD-5991 effectiveness, we achieved a high accuracy
354 amounting to an AUC of 0.89 and statistically significant discriminative performance for binary prediction with

355 ROC analysis (Fig. 5g). Altogether, our multi-parameter PPI data not only facilitates the construction of an
356 analysis model for the efficacy of BH3 mimetics, but also allows us to identify the relative contributions of
357 each assay data and the intricate balances among the protein complexes, potentially shedding light on the
358 drugs' modes of action.

359

360 **Using the PPI analysis model as a predictive biomarker for ABT-199 efficacy.**

361 We next explored whether BCL2 PPI profiling could proactively guide therapeutic decisions. BCL2 PPI
362 profiling was performed for ten patients who were treated with ABT-199 through oral administration.
363 Treatment outcomes were evaluated in accordance with European LeukemiaNet (ELN) recommendations[77],
364 and sequential samples were collected throughout the treatment journey (Fig. 6a and Supplementary Table
365 4).

366 For example, two patients, BC-6524 and BC-7230, exhibited contrasting patterns in our PPI profiling,
367 mirroring their disparate responses to ABT-199 treatment (Fig. 6b-d). Within the combination analysis model
368 detailed in Figure 4f, BC-6524 was anticipated to respond to a BCL2-targeted inhibitor with a high estimated
369 score of 0.90, while BC-7230 was predicted as a non-responder with an estimated score of 0.27 (Fig. 6b).
370 Specifically, BC-6524 displayed significantly higher counts for the BCL2-$BIM_{BH3}$ PBA and BCL2-BAX CPX
371 assays compared to BC-7230, while the BCLxL-BAK complex counts were low for both patients (Fig. 6c).
372 Impressively, these diagnostic predictions were strongly corroborated by the *in vivo* responses. For patient
373 BC-6524, peripheral blast counts began to decrease from day 2, culminating in confirmed complete
374 remission as per bone marrow examination (Fig. 6d, red). Conversely, patient BC-7230 did not respond to
375 ABT-199, as evidenced by increasing peripheral AML blasts from day 3 (Fig. 6d, grey).

376 When the 10 cases grouped into responsive (including complete remission and partial remission) and
377 non-responsive categories, our predictions for responder (R) and non-responder (NR) with a threshold score
378 of 0.61 aligned remarkably with the *in vivo* clinical outcomes for the nine patients (out of total ten patients),
379 including those for BC-6524 and BC-7230 previously described, achieving 100% sensitivity and 83%
380 specificity (Fig. 6d,e and Extended Data Fig. 10a-g). Moreover, the estimated scores for the initial responses
381 between the two groups manifested a significant difference as determined by the Mann-Whitney test, which
382 further increased when we included six additional samples from the same cohort collected after relapse (Fig.
383 6f and Extended Data Fig. 10h). An intriguing case was BC-7052, where our model initially projected a
384 favorable score of 0.64 (Extended Data Fig. 10a). After a short initial response, the patient entered partial
385 remission and ceased ABT-199 treatment. Interestingly, in *ex vivo* efficacy determination, the sample
386 recorded a high AUC value of 0.63, precisely mirroring the prediction by the analysis model (Supplementary
387 Table 4). This observation highlights a current model limitation, which was trained on *ex vivo* drug efficacy,
388 and suggests that incorporating factors unique to *in vivo* cancer evolution may refine the model's predictive
389 capabilities. For example, the BCLxL PBA count, absent from the current model, was conspicuously high for
390 BC-7052, hinting at a scenario where BCLxL proteins might become upregulated in activity as ABT-199
391 treatment persisted (Extended Data Fig. 10a, right).

392 In addition to the analysis of the BC-7064 case presented in Figure 4i, we conducted a longitudinal
393 tracking study on another case, BC-7107, to gain insights into AML evolution during ABT-199 treatment (Fig.

394 6g). This patient, who had relapsed refractory disease and previously undergone treatment with another
395 chemotherapeutic agent (Quizartinib), initially exhibited a robust BCL2 dependence (with an estimated score
396 of 0.93) (Fig. 6g-i). Notably, the patient achieved complete remission upon combined treatment with ABT-
397 199 and LDAC (Low-dose cytarabine) (Fig. 6g,j). However, after one month of treatment, relapse occurred
398 (Fig. 6j). Interestingly, PPI profiling after the relapse showed nearly background signals for all three
399 examined anti-apoptotic proteins, suggesting that the cancer might have developed a novel pathway to
400 evade apoptosis initiation (Fig. 6h-j).

401

402 ## Discussion

403 In our pursuit of establishing a precision medicine platform for protein complex-targeting therapies, we
404 harnessed the capabilities of the SMPC platform to comprehensively profile BCL2 family protein complexes
405 within specific AMLs. This endeavor involved optimizing extraction protocols applicable to clinical samples,
406 ensuring the preservation of most protein complexes and retaining specific BCL2 family protein
407 conformations through gentle lysis techniques. The integration of an anti-fouling polymer layer minimized
408 cross-interactions and non-specific adsorption during surface pull-down procedures. Additionally, the direct
409 single-molecule counting of target protein complexes demonstrated sustained sensitivity, effectively working
410 even when only a few hundred protein complexes were immobilized per imaging area (~$10^4$ μm²). These
411 technical innovations collectively enabled the assessment of over 20 distinct PPI species within clinical
412 samples comprising as few as ~$1.2 \times 10^6$ cells, achieving a level of sensitivity and accuracy amenable to
413 clinical applications.

414 Given that BH3 mimetics function as PPI inhibitors, conventional genomic and proteomic profiling
415 inherently falls short in capturing the dynamic rewiring of the PPI network and, consequently, predicting the
416 response to specific BH3 mimetics[46-49,78,79]. Indeed, our findings demonstrated that the counts of BCL2 family
417 protein complexes underwent drastic changes of more than three- to five-fold, while corresponding protein
418 levels exhibited marginal alterations approximately less than 30%. Moreover, the effect of the two examined
419 BH3 mimetics, ABT-199 and AZD-5991, on BCL2 family protein complexes appeared distinct, likely
420 attributed to their distinct mechanisms of action (as discussed below). This underscores how relying solely
421 on genomic mutations and proteomic levels, without considering their interconnectedness, may fail to fully
422 elucidate the intricate complexity of BCL2 family biology underlying BH3 mimetic efficacy.

423 Presently, there are competing hypotheses regarding the primary species of protein complexes that
424 BH3 mimetics target to dissociate for initiating apoptosis[16,80,81]. The activated BAX and BAK proteins,
425 responsible for forming BAX-BAK pores and mediating MOMP, can either be newly expressed by cells or
426 released from anti-apoptotic proteins. In the former scenario, BH3 mimetics saturate the target anti-apoptotic
427 proteins, preventing further sequestration of nascent BAX and BAK proteins. In the latter, BH3 mimetics bind
428 to the binding groove of anti-apoptotic proteins, causing the release of previously bound pro-apoptotic
429 proteins. A detailed analysis of changes in relevant protein complexes and protein levels, along with their
430 intricate balances, revealed that ABT-199 primarily acted by disassembling pre-existing BCL2 protein
431 complexes. Conversely, the MCL1 inhibitor AZD-5591 appeared to exert its efficacy by interfering with the
432 binding of newly produced BAK proteins to MCL1. Furthermore, tracing the behavior of the two types of
433 BCL2 protein complexes over time indicated that the dissociation of BCL2-BAX complexes – not BCL2-BIM

434 complexes – closely correlated with the onset of apoptosis in AML cells induced by ABT-199. Our findings
435 are consistent with previous studies that employed fluorescence lifetime imaging microscopy to observe the
436 release of BAD and BID, but not of BIM, from BCL2 and BCLxL by ABT-263[82]. Additionally, these studies
437 noted pro-apoptotic effects triggered by the disruption of BCLxL-BAX complexes through BAD in isolated
438 mouse liver mitochondria[83]. Indeed, in our multi-parametric measurement and linear regression analysis, the
439 quantity of BCL2-BAX complexes was more closely tied to the *ex vivo* efficacy of ABT-199 than BCL2-BIM
440 complexes. This led us to conclude that, in the specific AML cases studied, the dissociation of BCL2-BAX
441 complexes primarily drove the efficacy of ABT-199.

442 These data compelled us to hypothesize a particular group of driver protein complexes that powerfully
443 and positively correlated with the efficacy of the BH3 mimetics. We also found protein or PPI metrics
444 associated with the drug efficacy with negative coefficients, which we defined as resistance complexes. The
445 resulting analysis models included both driver and resistance complexes, reflecting the competing roles of
446 different anti-apoptotic proteins in achieving the BH3-mimetic efficacy. In the combined model for ABT-199
447 effectiveness, BCL2-BIM PBA and BCL2-BAX CPX worked as the driver complexes, while BCLxL-BAK CPX
448 worked as the resistance complex. However, the coefficient for BCLxL-BAK CPX was much smaller than
449 those of BCL2-related parameters, consistent with the singular dependence of AMLs on BCL2. On the other
450 hand, the analysis model for AZD-5591 efficacy, consisting of MCL1 total level, BCLxL-BAK CPX, and
451 BCLxL-$BIM_{BH3}$ PBA, assigned larger coefficients to two BCLxL-involved parameters than it did for the MCL1
452 total level, suggesting that MCL1 was in direct competition with BCLxL in mediating the effectiveness of
453 AZD-5591. It is important to note that our current suite of assays lacks the capability to detect certain anti-
454 and pro-apoptotic proteins in the BCL2 family, including BFL1 and BID. By extending our assay to
455 incorporate these proteins – achievable through the screening of appropriate antibodies for IP and detection
456 – we anticipate a more comprehensive profiling of the BCL2 family PPI network, as well as enhanced
457 accuracy in our analysis model.

458 Our analysis model bears an intrinsic limitation as it was constructed based on drug efficacy
459 determined *ex vivo*. Additionally, due to the relatively small size of the patient cohort employed in this study,
460 the applicability of the model to larger cohorts remains untested. Notwithstanding these considerations, we
461 took the step of applying the analysis model for prospective stratification of ABT-199 responders.
462 Remarkably, in nine out of ten cases, predictions based on three PPI metrics showed a significant correlation
463 with clinical responses, achieving 100% sensitivity and 83.3% specificity. Additionally, our longitudinal
464 tracking approach allowed us to observe how PPI connectivity evolved among the BCL2 family proteins,
465 ultimately contributing to the development of resistance and cancer recurrence. While obtaining frozen
466 BMMC or PBMC samples from hematological malignancies does not present significant challenges, we
467 expect that the extraction of protein complexes from fixed tissues will be a crucial technical factor for
468 successfully extending this method to solid tumors. Furthermore, ready access to the surface-passivated
469 reaction chip and the single-molecule imaging device used in this study is essential for the widespread
470 adoption of this diagnostic method in clinical decision-making.

471 In summary, our findings advocate for the SMPC platform as an effective method of scrutinizing
472 multiple protein complexes in clinical samples with heightened sensitivity and precision. While emerging
473 technologies such as single protein sequencing primarily serve as discovery tools[84], the platform showcased
474 in this study is tailored to the examination of dozens of protein complexes in clinical specimens. These

475 profiles distill into information that is most directly pertinent to drug efficacies, thereby facilitating treatment
476 decisions that would be considerably challenging to achieve through genomic and proteomic profiling alone.
477 Given the rise in protein complex-targeting therapies, it will be intriguing to see whether the methodologies
478 established herein could be extended to address other disease-associated protein complexes and drugs
479 beyond the BCL2 family and BH3 mimetics.

480 # Methods

481 **Antibodies**

482 Anti-rabbit immunoglobulin G (IgG) with biotin conjugation (111-065-144; Jackson ImmunoResearch) and
483 anti-mouse immunoglobulin G (IgG) with biotin conjugation (715-066-151; Jackson ImmunoResearch) were
484 used to immobilize the antibodies for surface IP. Anti-RFP antibody with biotin conjugation (ab34771;
485 Abcam) and anti-GFP antibody with biotin conjugation (ab6658; Abcam) were used to immobilize mCherry-
486 or eGFP-labeled proteins on surface. Anti-MCL1 (94296S; Cell Signaling Technology), BCLxL (MA5-15142;
487 Thermo Fisher Scientific), BCL2 (4223S; Cell Signaling Technology), BAX (5023S; Cell Signaling
488 Technology), and BAK (ab32371; Abcam) antibodies were used to immobilize the corresponding proteins via
489 surface pull-down. Anti-MCL1 (MAB8825; Abnova), BCLxL (NBP1-47665; Novus Biologicals), BCL2 (sc-
490 7382; Santa Cruz Biotechnology), BAX (MABC1176M; Sigma Aldrich), BAK (sc-517390; Santa Cruz
491 Biotechnology), BIM (sc-374358; Santa Cruz Biotechnology), BAD (sc-8044; Santa Cruz Biotechnology),
492 NOXA (sc-56169; Santa Cruz Biotechnology) antibodies were used to detect the corresponding proteins in
493 the protein total level and the protein complex assays. To measure BCL2-BAX complex level, anti-BAX
494 (5023S; Cell Signaling Technology) and anti-BCL2 (BMS1028; Invitrogen) antibodies were used to
495 immobilize and detect the BCL2-BAX complex, respectively. Anti-rabbit immunoglobulin G (IgG) with Cy3
496 conjugation (111-165-046; Jackson ImmunoResearch) and anti-mouse IgG with Cy3 conjugation (715-165-
497 151; Jackson ImmunoResearch) were used to label the detection antibodies for immunoassay. Anti-BCL2
498 antibody (BMS1028; Invitrogen), mouse IgG1 kappa isotype control (554121; BD Biosciences), and anti-
499 mouse immunoglobulin G (IgG) with PE conjugation (715-116-150; Jackson ImmunoResearch) were used to
500 detect the protein levels for quantitative flow cytometry.

501

502 **Drug reagents**

503 Staurosporine (HY-15141; MedChemExpress), ABT-199 (HY-15531; MedChemExpress), and AZD-5991 (C-
504 1060; Chemgood) were used to treat the blood cancer cell lines or primary AML cells. The drugs were
505 diluted to 10 mM with DMSO and stored at -80 °C.

506

507 **Cell culture**

508 HL60, THP-1, U937, and Ramos cells were purchased from Korean Cell Line Bank. HEK293T and SU-DHL8
509 cells were purchased from American Type Culture Collection (ATCC). NB4 cells were purchased from
510 German Collection of Microorganisms and Cell Cultures (DSMZ). PC9 cells were provided by Y. Hayata
511 (Kyushu University Faculty of Medicine, Japan). HEK293T cells were cultured in DMEM (D6429; Sigma
512 Aldrich) supplemented with 10% (v/v) FBS (26140-079; Gibco) and 100 μg/ml penicillin/streptomycin (15140-
513 122; Gibco). HL60, THP-1, NB4, U937, Ramos, SU-DHL8, and PC9 cells were cultured in RPMI1640
514 (R8758; Sigma Aldrich) supplemented with 10 % (v/v) FBS and 100 μg/ml penicillin/streptomycin. For THP-1,
515 0.05 mM of 2-mercaptoethanol (M3148; Sigma Aldrich) was added to culture media. All cells were incubated
516 in a humidified incubator at 37 °C, 5% $CO_2$. HEK293T and PC9 cells were rinsed with cold DPBS (D8537;
517 Sigma Aldrich) before collection. Cells were collected with the scraper (90020; SPL Life Sciences) in 1 ml of
518 cold DPBS. Suspension-type cells were collected with centrifugation at 500 g for 5 minutes at 4 °C and
519 rinsed with 1 ml of cold DPBS. The cell suspensions were centrifuged at 500 g for 5 minutes at 4 °C. The
520 supernatants were discarded after centrifugation and the cell pellets were stored at -80 °C by snap-freezing
521 with liquid nitrogen.

522

523 **Primary AML samples**

524 The cryo-preserved bone marrow mononuclear cells (BMMCs) and peripheral blood mononuclear cells
525 (PBMCs) collected from AML patients treated at Seoul National University Hospital were used.
526 Samples were collected between January 2014 and December 2019. Acute promyelocytic leukemias and
527 biphenotypic leukemias were excluded. Mononuclear cells were isolated by ficoll gradient centrifugation. All
528 samples were frozen in liquid nitrogen before flow cytometry and SMPC analysis. Aforementioned cell line
529 collection protocol was applied for primary AML cell collection. Culturing method for flow cytometry assay is
530 described on the sub-section on Drug treatment and drug efficacy measurement. Detailed information of
531 each sample is described in Supplementary Table 1. This study was conducted according to the Declaration
532 of Helsinki and was approved by the institutional review board of Seoul National University Hospital (IRB
533 number: H-1910-176-107).

534

535 **Fluorescence-labeled protein constructions**

536 All full-length BCL2 family proteins (*BCL2* (HG10195-M; SinoBiological), *BCLxL* (HG10455-M;
537 SinoBiological), *MCL1* (HG10240-M; SinoBiological), $BIM_{EL}$ (HG13816-G; SinoBiological), *BAD* (HG10020-
538 M; SinoBiological), *BAX* (HG11619-M; SinoBiological), *BAK* (HG10450-M; SinoBiological) and *NOXA*
539 (HG16548-U; SinoBiological)) were isolated from their respective human cDNA. cDNA of $BIM_{BH3}$
540 (MRQAEPADMRPEIWIAQELRRIGDEFNAYYARR) was isolated from $BIM_{EL}$ cDNA. cDNA of *BAK fragments*
541 – residues 24-69 ($\alpha_1$ helix), 70-91 ($\alpha_2$-$\alpha_3$ helices), 90-150 ($\alpha_3$-$\alpha_5$ helices), and 146-187 ($\alpha_6$-$\alpha_8$ helices) – were
542 isolated from *BAK* cDNA. All cDNAs were cloned into *pCMV* vectors with either eGFP or mCherry sequences
543 to generate fluorescence-labeled proteins using Gibson assembly. The fluorescence proteins were fused to
544 the carboxyl- end of BCL2 family proteins. The resulting plasmids were introduced into HEK293T cells
545 through transient transfection. Plasmid DNA with the amount of 10 μg was mixed with 30 μg of linear
546 polyethyleneimine (PEI) (23966-100; Polysciences) in 1 ml of serum-free DMEM. The mixture was
547 introduced into ~$2x10^6$ of HEK293T cells in a 90 $mm^2$ cell culture plate.

548

549 **Cell lysis**

550 All collected cell pellets were resuspended with the lysis buffer (0.2% or 1% (v/v) detergent, 50 mM HEPES
551 with pH 7.4, 150 mM NaCl, 10% (v/v) glycerol, 1 mM EDTA, 2% (v/v) protease inhibitor cocktail (P8340;
552 Sigma Aldrich), 2% (v/v) phosphatase inhibitor cocktail 2 (P5726; Sigma Aldrich), and 2% (v/v) phosphatase
553 inhibitor cocktail 3 (P0044; Sigma Aldrich). Triton-X100 (X100; Sigma Aldrich), glyco-diosgenin (GDN)
554 (GDN101; Anatrace), digitonin (D141; Sigma Aldrich), Tween 20 (P2287; Sigma Aldrich), 3-[(3-
555 Cholamidopropyl) dimethylammonio]-1-propanesulfonate hydrate (CHAPS) (C3023; Sigma Aldrich), and
556 sodium dodecyl sulfate (SDS) (L3771; Sigma Aldrich)) were used for optimizing the lysis protocol. Triton-
557 X100, GDN, digitonin, Tween 20, and CHAPS were used in 1% (v/v), and SDS was used in 0.2% (v/v) in
558 lysis buffer. HEK293T cells expressing probes for the PBA experiments – $BIM_{BH3}$-eGFP, $BIM_{EL}$-eGFP, BAD-
559 eGFP, and NOXA-eGFP – were lysed with Triton-X100 lysis buffer. HEK293T cells expressing fluorescence
560 protein labeled BCL2 family proteins (BCL2-mCherry, BCLxL-mCherry, MCL1-mCherry, BCL2-eGFP,
561 BCLxL-eGFP, MCL1-eGFP, BAX-eGFP, BAK-eGFP, and BAK fragments-eGFP) were lysed with GDN lysis
562 buffer for immunoassay and PBA. The construct designs and protein expressions in HEK293T cells for

563 fluorescence protein labeled BCL2 family proteins are described on above. All the cancer cell lines, and
564 primary AML cells were lysed with GDN lysis buffer for immunoassay and PBA.
565 For the cell lysis, the cell pellets were resuspended with the designated lysis buffer and incubated for 30
566 minutes at 4 °C. After lysis, the cell suspensions were centrifuged at 15,000 g for 10 minutes at 4 °C. The
567 supernatants were isolated after centrifugation. The total protein concentration for each supernatant was
568 measured with a DC protein assay kit (5000113, 5000114, 5000115; Bio-Rad) following the manufacturer's
569 instructions. The total concentration of the fluorescence proteins in each supernatant was measured with a
570 Sense microplate reader (425-301; HIDEX). To quantify the fluorescence proteins, a laser wavelength of 485
571 nm was used for eGFP excitation and 544 nm was used for mCherry excitation respectively. Serial dilution
572 experiments using eGFP and mCherry were performed to generate the calibration curves. The
573 aforementioned calibration curves were used to quantify the concentrations of fluorescently labeled proteins.
574 The supernatants were then aliquoted and stored at -80 °C followed by snap-freezing with liquid nitrogen.
575
576 **Drug treatment and drug efficacy measurement**
577 All blood cancer cells and primary AML cells were precultured in a 25T flask (non-treated surface) for 3 hours
578 before drug treatment. All cells were seeded in 4.5 ml of culture media and cultured in a humidified incubator
579 at 37 °C, 5% $CO_2$. STS, ABT-199, and AZD-5991 were then treated to cells at various concentrations. All
580 drugs were initially diluted with DMSO to 1 mM. For experiments, serial dilution was performed with non-
581 serum RPMI1640 to reach the target concentration. To determine the efficacy of drugs in blood cancer cells
582 and primary AML cells, an AnnexinV/PI apoptosis assay was performed, where cells were stained with FITC-
583 AnnexinV (640906; Biolegend) and PI (421301; Biolegend). After drug treatment, $5x10^5$ of cells were rinsed
584 with cold DPBS and collected by centrifugation with 500 g for 5 minutes at 4 °C. After the supernatants were
585 discarded, the cell pellets were resuspended with 100 µl of cold AnnexinV-binding buffer (422201;
586 Biolegend). After resuspension, 10 µl of FITC-AnnexinV solution and 5 µl of PI solution were added into the
587 cell suspensions. The cell suspensions were incubated for 15 minutes at room temperature avoiding
588 exposure to light. After that, 400 µl of cold AnnexinV-binding buffer was added to avoid overstaining. The
589 stained cells were analyzed with a flow cytometry (SH800S; Sony). The proportions of $AnnexinV^-/PI^-$ cells
590 from each sample were calculated and converted to viability (%). Based on the measured viability, the drug
591 efficacy curve was fitted using the *logistic* function inside the analysis software (OriginPro 2022), and the
592 area under curve (AUC) was measured from the fitted curve.
593
594 **Single-molecule pull-down and co-IP for BCL2 family proteins**
595 5 µg/ml of NeutrAvidin (31000; Thermo Fisher Scientific) was loaded into each reaction chamber of the Pi-
596 Chip (PROTEINA) and incubated for 10 minutes. The imaging chip was washed with TritonX-100-buffer
597 (0.1% (v/v) TritonX-100, 50 mM HEPES with pH 7.4, 150 mM NaCl) to remove unbound NeutrAvidin. Biotin-
598 conjugated IgGs (anti-rabbit IgGs) were loaded to each reaction chamber with 1:200 in TritonX-100-buffer
599 and incubated for 10 minutes, followed by washing with TritonX-100-buffer. Then, the previously mentioned
600 monoclonal antibodies (anti-MCL1, BCLxL, BCL2, BAX, and BAK antibodies for surface IP) were introduced
601 into each reaction chamber at a dilution of 1:100 in TritonX-100-buffer, and then incubated for a duration of
602 10 minutes. The imaging chip was washed with GDN-buffer (0.01% (w/v) GDN, 50 mM HEPES with pH 7.4,
603 150 mM NaCl, 1% (v/v) Glycerol, 1 mM EDTA). After washing, crude cell extracts were diluted based on the
604 total protein concentrations and were loaded into each reaction chamber. During the process of

605 immunoprecipitating fluorescence-labeled proteins, anti-RFP or anti-GFP antibodies were introduced at a
606 dilution of 1:200 in TritonX-100-buffer. This mixture was then incubated for a period of 20 minutes, as an
607 alternative to using biotin-conjugated IgGs.
608 To measure the total level of BCL2 family proteins, cell extracts with a concentration of 1 mg/ml were
609 introduced into each reaction chamber. These chambers were pre-coated with primary antibodies for
610 immunoprecipitation, and the samples were allowed to incubate for 1 hour to capture of the target proteins.
611 To measure the total level of BAX and BAK, the cell extracts were mixed with the activation buffer (2% (v/v)
612 Triton X-100, 50 mM HEPES (pH 7.4), 150 mM NaCl, and 1 mM EDTA) with 1:1 for 30 minutes before pull-
613 down. After activation, the cell extracts were loaded into each reaction chamber and incubated for 1 hour. To
614 measure the PPI complex levels, 2 mg/ml of cell extracts were loaded into each reaction chamber with 2
615 hours of incubation period to pull-down the target PPI complexes.
616 After the surface pull-down of target proteins or protein complexes, the previously mentioned primary
617 antibodies were introduced for the purpose of detecting either total protein levels (anti-MCL1, BCLxL, BCL2,
618 BAX, and BAK antibodies for immunoassay) or protein complexes (anti-BAX, BAK, BIM, BAD, and NOXA
619 antibodies for immunoassay). These antibodies were loaded into each reaction chamber at a dilution of
620 1:100 in TritonX-100-buffer and then incubated for a duration of 1 hour. To label the detection antibodies,
621 Cy3-conjugated IgGs (anti-mouse IgGs) were introduced into each reaction chamber at a dilution of 1:1,000
622 in TritonX-100-buffer. These chambers underwent an incubation period of 20 minutes.
623 To measure the PBA, 1 mg/ml of cell extracts were loaded into each reaction chamber and incubated for 1
624 hour. After that, the imaging chip was washed with GDN-buffer. The HEK293T cells expressing PBA probes
625 were lysed with TritonX-100 lysis buffer. The crude cell extracts containing the PPI probes were diluted to
626 achieve the target eGFP concentration. Subsequently, they were incubated for a duration of 10 minutes with
627 the immunoprecipitated bait proteins.
628
629 **Single-molecule fluorescence imaging**
630 Single-molecule fluorescence signal was assessed using the Pi-View system (PROTEINA), which allows for
631 single-molecule fluorescence imaging at two different excitation lasers, 488 nm and 532 nm[55,57,65]. The
632 emitted photons from a single fluorophore were collected by employing a sensitive sCMOS (scalable
633 complementary metal-oxide semiconductor) camera. An autofocus system provides high throughput image
634 acquisition across the whole imaging chip that contained 40 reaction chambers. To determine the single-
635 molecule counts for each assay, ~10 different locations were imaged in a single reaction chamber. Each
636 image was acquired for 5 frames with 100 ms time resolution, and those frames were averaged to generate
637 a single snapshot, which reduced random noise and improved singal-to-noise ratio. Protocols for image
638 processing were detailed in Extended Data Fig. 2. The current imaging system identifies and counts up to
639 12,000 single-molecule fluorescence spots within a 100×100 μm² field of view, an upper limit for the
640 identification of diffraction-limited spots. When the number of such spots exceeds this limit, overlapping
641 begins to occur, compromising the ability to identify individual spots (Extended Data Fig. 2d). To address this
642 limitation, the total fluorescence signals captured across all pixels within the field of view were integrated.
643 Simultaneously, by recording time-traces of photobleaching, a relationship between the number of single-
644 molecule spots and the total fluorescence intensity was established, particularly, in the range that permitted
645 the identification of individual spots (i.e., below the upper limit), which was typically linear (Extended Data
646 Fig. 2e,f). This linear relationship ultimately enabled extrapolation of total fluorescence intensity into

corresponding single-molecule counts in regions exceeding the upper limit (Extended Data Fig. 2g). The computational analysis codes are available on our GitHub.

**Drug efficacy prediction model analysis**

Drug efficacy prediction models for AML patients were generated using linear regression analysis by MATLAB 2021a. The protein and protein complex data from the primary AML cells were all converted to a $log_2$ scale. Any instance where the number of single-molecule fluorescence spots was less than 100 counts were fixed to the minimum value of 100 counts for log transformation. For BCLxL-BAX, BCLxL-BAK, and BCL2-BAK protein complexes, the total fluorescence signal data were used instead of single-molecule spot data, and the fluorescence signals less than $10^7$ were fixed to the minimum value ($10^7$ A.U.) for log transformation. The *ex vivo* drug efficacy (*ex vivo* AUC) of the primary AML cells were obtained from the vaibility measuring method described on the sub-section on Drug treatment and drug efficacy measurement. The area under curves (AUCs) were initially calculated from the fitted curves for viability after BH3 mimetic treatment, and *ex vivo* drug efficacy were normalized by *ex vivo AUC=1-(AUC/Maximal AUC)*. The correlation between the PPI profiling data and the *ex vivo* drug efficacy was calculated through linear regression with the custom analysis code. Each generated model provided the statistical indicators, *p*-values for the linear regression itself, as well as for the intercept. The models were accepted only when their *p*-values were statistically significant (*p*-value<0.05). To construct combined metrics models, various randomly selected combinations of PPI profiles were assessed in order to identify a model that met two criteria: high correlation (indicated by a high R value) and statistical significance (with *p*-values < 0.05). Lasso regression analysis for selecting metrics which are highly correlated with drug response were generated by Python 3.11. The training and test groups were randomly selected from the primary AML sample cohort. The Lasso regression models were trained using the training group and evaluated based on Pearson's R as well as prediction outcomes for the test group, and 67 models were selected from 10,000 different initial models (Extended Data Fig. 8d). The custom analysis codes and raw data utilized for generating the models can be accessed on our Github.

**BH3 profiling**

We followed the methods outlined in the previous studies for BH3 profiling[74,75]. The MEB buffer (150 mM mannitol (M9647; Sigma Aldrich), 10 mM HEPES pH 7.4, 50 mM KCl (P9541; Sigma Aldrich), 0.02 mM EGTA (BE004; Biosolution), 0.02 mM EDTA, 0.1% (w/v) BSA (A4737; Sigma Aldrich), and 5 mM succinate (S3674; Sigma Aldrich)), along with the staining solution (20 μg/ml oligomycin (O4876; Sigma Aldrich), 50 μg/ml digitonin, 2 μM JC-1 (ENZ-52304; Enzo Life Sciences), and 10 mM 2-mercaptoethanol (M3148; Sigma Aldrich) in the MEB buffer) were prepared and stored at 4 °C. The BH3 peptides (or BH3 mimetics) were diluted with the staining solution to achieve twice the target concentration, producing the 2x staining solution for each peptide. The synthesized BH3 peptides (BIM (MRPEIWIAQELRRIGDEFNA, purity=98%), BAD (LWAAQRYGRELRRMSDEFEGSFKGL, purity=99%), and HRK (SSAAQLTAARLKALGDELHQY, purity=99%) all synthesized by PEPTRON (South Korea)), DMSO, carbonyl cyanide 4-(trifluoromethoxy) phenylhydrazone (FCCP) (C2920; Sigma Aldrich), ABT-199, and AZD-5991 were used for BH3 profiling. We aliquoted 50 μl of the 2x staining solution into a black-coated 96-well plate to produce a BH3 profiling plate, which was then stored at -80 °C until use.

688 To perform BH3 profiling for primary AML cells, $10^6$ of primary AML cells were rinsed with 1 ml of RPMI1640
689 supplemented with 10% (v/v) FBS. After centrifugation at 300 g for 5 minutes, the collected cells were
690 resuspended in 1 ml of MEB buffer. Subsequently, the resuspended cells were then aliquoted into each well
691 of the BH3 profiling plate that had been equilibrated to room temperature. The BH3 profiling plate was placed
692 in a plate reader (Synergy H1; BioTek) set at a constant temperature of 32°C, and the fluorescence was
693 measured every 5 minutes over a period of 3 hours. To measure the relative fluorescence units (RFU) at a
694 wavelength of 590 nm, a light wavelength of 545 nm was used for JC-1 excitation. Based on the measured
695 RFU, the area under the curve (AUC) was measured using the analysis software (OriginPro 2022). The
696 depolarizations were calculated by the following equation, and the BH3 profiling results for primary AML cells
697 can be found in Supplementary Information.

698 $$Depolarization = 1 - \frac{AUC_{sample} - AUC_{FCCP}}{AUC_{DMSO} - AUC_{FCPP}}$$

699

700 **Quantitative flow cytometry**

701 We employed the methods outlined in previous studies to quantify protein levels using flow cytometry[85].
702 Briefly, $10^6$ of primary AML cells were rinsed with 1 ml of RPMI1640 supplemented with 10% (v/v) FBS and
703 collected with centrifugation at 300 g for 5 minutes. The collected cells were resuspended in 0.5 ml of 37 °C
704 lyse fix buffer (558049; BD Biosciences). The cell suspensions were centrifuged at 1,700 g for 5 minutes,
705 after which the supernatants were discarded. The cell pellets were resuspended in staining wash buffer
706 (0.5% (w/v) BSA and 0.1% (w/v) sodium azide (S2002; Sigma Aldrich) in DPBS) and aliquoted into two
707 separate tubes at 100 µl each. 900 µl of permeabilization wash buffer (PW) (557885; BD Biosciences) was
708 then added to each tube, followed by a 10-minute incubation at room temperature. Following the incubation,
709 the tubes were subjected to centrifugation at 1,700 g for 5 minutes, and the supernatant was subsequently
710 reduced to 100 µl. The permeabilized cells were stained with either 0.5 µg of anti-BCL2 antibody or an
711 isotype control antibody respectively and incubated for 30 minutes. The cells were rinsed by adding 900 µl of
712 PW and centrifuged at 1,700 g for 5 minutes. The rinsed cells were then stained with 1.5 µl of PE-conjugated
713 anti-Mouse IgG and incubated for 30 minutes in a dark room to prevent light exposure. After rinsing to
714 eliminate any unbound antibodies, the stained cells were resuspended in 350 µl of fix buffer (557870; BD
715 Biosciences) for fixation and stored at 4°C until they were ready to be analyzed using a flow cytometer
716 (SH800S; Sony). Quantum™ R-PE MESF beads (827; Bangs Laboratories) were utilized to produce
717 calibration curves. These curves were subsequently employed, following the manufacturer's instructions, to
718 quantify the levels of BCL2 in the samples.

719

720 **Reporting Summary**. Further information on research design is available in the Nature Research Reporting
721 Summary linked to this article.

722

723 **Data availability**

724 The data supporting the findings of this study are available within the article and its Supplementary
725 Information. All raw data generated or analysis during the study are available on the Github at the following
726 link: https://github.com/tyyoonlab-snu/Nat-Biomed-Eng-2023-.

727

728 **Code availability**

729 The custom MATLAB and Python codes used for drug efficacy prediction model analysis are available on the
730 Github at the following link: https://github.com/tyyoonlab-snu/Nat-Biomed-Eng-2023-
731
732

733 ## References


734 1 Alberts, B. The cell as a collection of protein machines: Preparing the next generation of molecular
735 biologists. *Cell* **92**, 291-294, doi:Doi 10.1016/S0092-8674(00)80922-8 (1998).
736 2 Li, M. X. *et al.* BAK alpha6 permits activation by BH3-only proteins and homooligomerization via the
737 canonical hydrophobic groove. *Proc Natl Acad Sci U S A* **114**, 7629-7634,
738 doi:10.1073/pnas.1702453114 (2017).
739 3 Saxton, R. A. & Sabatini, D. M. mTOR Signaling in Growth, Metabolism, and Disease (vol 168, pg
740 960, 2017). *Cell* **169**, 362-362, doi:10.1016/j.cell.2017.03.035 (2017).
741 4 Broz, P. & Dixit, V. M. Inflammasomes: mechanism of assembly, regulation and signalling. *Nat Rev*
742 *Immunol* **16**, 407-420, doi:10.1038/nri.2016.58 (2016).
743 5 Kale, J., Osterlund, E. J. & Andrews, D. W. BCL-2 family proteins: changing partners in the dance
744 towards death. *Cell Death Differ* **25**, 65-80, doi:10.1038/cdd.2017.186 (2018).
745 6 Kalkavan, H. & Green, D. R. MOMP, cell suicide as a BCL-2 family business. *Cell Death Differ* **25**,
746 46-55, doi:10.1038/cdd.2017.179 (2018).
747 7 Wei, M. C. *et al.* Proapoptotic BAX and BAK: a requisite gateway to mitochondrial dysfunction and
748 death. *Science* **292**, 727-730, doi:10.1126/science.1059108 (2001).
749 8 Chipuk, J. E., Bouchier-Hayes, L. & Green, D. R. Mitochondrial outer membrane permeabilization
750 during apoptosis: the innocent bystander scenario. *Cell Death Differ* **13**, 1396-1402,
751 doi:10.1038/sj.cdd.4401963 (2006).
752 9 Moore, V. D. & Letai, A. BH3 profiling - Measuring integrated function of the mitochondrial apoptotic
753 pathway to predict cell fate decisions. *Cancer Lett* **332**, 202-205, doi:10.1016/j.canlet.2011.12.021
754 (2013).
755 10 Ku, B., Liang, C. Y., Jung, J. U. & Oh, B. H. Evidence that inhibition of BAX activation by BCL-2
756 involves its tight and preferential interaction with the BH3 domain of BAX. *Cell Res* **21**, 627-641,
757 doi:10.1038/cr.2010.149 (2011).
758 11 Willis, S. N. *et al.* Proapoptotic Bak is sequestered by Mcl-1 and Bcl-x(L), but not Bcl-2, until
759 displaced by BH3-only proteins. *Gene Dev* **19**, 1294-1305, doi:10.1101/gad.1304105 (2005).
760 12 Sarosiek, K. A. *et al.* BID Preferentially Activates BAK while BIM Preferentially Activates BAX,
761 Affecting Chemotherapy Response. *Mol Cell* **51**, 751-765, doi:10.1016/j.molcel.2013.08.048 (2013).
762 13 Robin, A. Y. *et al.* Crystal structure of Bax bound to the BH3 peptide of Bim identifies important
763 contacts for interaction. *Cell Death Dis* **6**, doi:ARTN e180910.1038/cddis.2015.141 (2015).
764 14 Ren, D. *et al.* BID, BIM, and PUMA are essential for activation of the BAX- and BAK-dependent cell
765 death program. *Science* **330**, 1390-1393, doi:10.1126/science.1190217 (2010).
766 15 Czabotar, P. E. *et al.* Bax Crystal Structures Reveal How BH3 Domains Activate Bax and Nucleate
767 Its Oligomerization to Induce Apoptosis. *Cell* **152**, 519-531, doi:10.1016/j.cell.2012.12.031 (2013).
768 16 Westphal, D., Kluck, R. M. & Dewson, G. Building blocks of the apoptotic pore: how Bax and Bak are
769 activated and oligomerize during apoptosis. *Cell Death Differ* **21**, 196-205, doi:10.1038/cdd.2013.139
770 (2014).

771 17 Zou, Z. L., Tao, T., Li, H. M. & Zhu, X. mTOR signaling pathway and mTOR inhibitors in cancer:
772 progress and challenges. *Cell Biosci* **10**, doi:10.1186/s13578-020-00396-1 (2020).
773 18 Laplante, M. & Sabatini, D. M. mTOR Signaling in Growth Control and Disease. *Cell* **149**, 274-293,
774 doi:10.1016/j.cell.2012.03.017 (2012).
775 19 Shen, H. H. *et al.* NLRP3: A promising therapeutic target for autoimmune diseases. *Autoimmun Rev*
776 **17**, 694-702, doi:10.1016/j.autrev.2018.01.020 (2018).
777 20 Heneka, M. T., McManus, R. M. & Latz, E. Inflammasome signalling in brain function and
778 neurodegenerative disease. *Nat Rev Neurosci* **19**, 610-621, doi:10.1038/s41583-018-0055-7 (2018).
779 21 Um, H. D. Bcl-2 family proteins as regulators of cancer cell invasion and metastasis: a review
780 focusing on mitochondrial respiration and reactive oxygen species. *Oncotarget* **7**, 5193-5203,
781 doi:DOI 10.18632/oncotarget.6405 (2016).
782 22 Kelly, P. N. & Strasser, A. The role of Bcl-2 and its pro-survival relatives in tumourigenesis and
783 cancer therapy. *Cell Death Differ* **18**, 1414-1424, doi:10.1038/cdd.2011.17 (2011).
784 23 Hockings, C. *et al.* Mcl-1 and Bcl-x(L) sequestration of Bak confers differential resistance to BH3-
785 only proteins. *Cell Death Differ* **25**, 721-734, doi:10.1038/s41418-017-0010-6 (2018).
786 24 Lu, H. Y. *et al.* Recent advances in the development of protein-protein interactions modulators:
787 mechanisms and clinical trials. *Signal Transduct Tar* **5**, doi:ARTN 21310.1038/s41392-020-00315-3
788 (2020).
789 25 Cory, S., Roberts, A. W., Colman, P. M. & Adams, J. M. Targeting BCL-2-like Proteins to Kill Cancer
790 Cells. *Trends Cancer* **2**, 443-460, doi:10.1016/j.trecan.2016.07.001 (2016).
791 26 Ashkenazi, A., Fairbrother, W. J., Leverson, J. D. & Souers, A. J. From basic apoptosis discoveries
792 to advanced selective BCL-2 family inhibitors. *Nat Rev Drug Discov* **16**, 273-284,
793 doi:10.1038/nrd.2016.253 (2017).
794 27 Billard, C. BH3 Mimetics: Status of the Field and New Developments. *Mol Cancer Ther* **12**, 1691-
795 1700, doi:10.1158/1535-7163.Mct-13-0058 (2013).
796 28 Tse, C. *et al.* ABT-263: A potent and orally bioavailable Bcl-2 family inhibitor. *Cancer Res* **68**, 3421-
797 3428, doi:10.1158/0008-5472.Can-07-5836 (2008).
798 29 Souers, A. J. *et al.* ABT-199, a potent and selective BCL-2 inhibitor, achieves antitumor activity while
799 sparing platelets. *Nat Med* **19**, 202-208, doi:10.1038/nm.3048 (2013).
800 30 Stilgenbauer, S. *et al.* Venetoclax in relapsed or refractory chronic lymphocytic leukaemia with 17p
801 deletion: a multicentre, open-label, phase 2 study. *Lancet Oncol* **17**, 768-778, doi:10.1016/S1470-
802 2045(16)30019-5 (2016).
803 31 Wei, A. H. *et al.* Venetoclax Combined With Low-Dose Cytarabine for Previously Untreated Patients
804 With Acute Myeloid Leukemia: Results From a Phase Ib/II Study. *J Clin Oncol* **37**, 1277-1284,
805 doi:10.1200/JCO.18.01600 (2019).
806 32 DiNardo, C. D. *et al.* Venetoclax combined with decitabine or azacitidine in treatment-naive, elderly
807 patients with acute myeloid leukemia. *Blood* **133**, 7-17, doi:10.1182/blood-2018-08-868752 (2019).
808 33 Townsend, P. A., Kozhevnikova, M. V., Cexus, O. N. F., Zamyatnin, A. A. & Soond, S. M. BH3-
809 mimetics: recent developments in cancer therapy. *J Exp Clin Canc Res* **40**, doi:ARTN
810 35510.1186/s13046-021-02157-5 (2021).
811 34 Jameson, J. L. & Longo, D. L. Precision Medicine - Personalized, Problematic, and Promising. *New*
812 *Engl J Med* **372**, 2229-2234, doi:10.1056/NEJMsb1503104 (2015).

813 35 Seymour, J. F. *et al.* Bcl-2 Inhibitor ABT-199 (GDC-0199) Monotherapy Shows Anti-Tumor Activity
814 Including Complete Remissions In High-Risk Relapsed/Refractory (R/R) Chronic Lymphocytic
815 Leukemia (CLL) and Small Lymphocytic Lymphoma (SLL). *Blood* **122** (2013).
816 36 Roberts, A. W. *et al.* Targeting BCL2 with Venetoclax in Relapsed Chronic Lymphocytic Leukemia.
817 *New Engl J Med* **374**, 311-322, doi:10.1056/NEJMoa1513257 (2016).
818 37 Konopleva, M. *et al.* Efficacy and Biological Correlates of Response in a Phase II Study of
819 Venetoclax Monotherapy in Patients with Acute Myelogenous Leukemia. *Cancer Discov* **6**, 1106-
820 1117, doi:10.1158/2159-8290.CD-16-0313 (2016).
821 38 Pollyea, D. A. *et al.* Venetoclax in Combination with Hypomethylating Agents Induces Rapid, Deep
822 and Durable Responses in Patients with AML Ineligible for Intensive Therapy. *Blood* **132**,
823 doi:10.1182/blood-2018-99-117179 (2018).
824 39 Guieze, R. *et al.* Mitochondrial Reprogramming Underlies Resistance to BCL-2 Inhibition in
825 Lymphoid Malignancies. *Cancer Cell* **36**, 369-384 e313, doi:10.1016/j.ccell.2019.08.005 (2019).
826 40 Thijssen, R. *et al.* Resistance to ABT-199 induced by microenvironmental signals in chronic
827 lymphocytic leukemia can be counteracted by CD20 antibodies or kinase inhibitors. *Haematologica*
828 **100**, e302-306, doi:10.3324/haematol.2015.124560 (2015).
829 41 Ruvolo, P. P., Deng, X. & May, W. S. Phosphorylation of Bcl2 and regulation of apoptosis. *Leukemia*
830 **15**, 515-522, doi:10.1038/sj.leu.2402090 (2001).
831 42 Yip, K. W. & Reed, J. C. Bcl-2 family proteins and cancer. *Oncogene* **27**, 6398-6406,
832 doi:10.1038/onc.2008.307 (2008).
833 43 Blombery, P. *et al.* Acquisition of the Recurrent Gly101Val Mutation in BCL2 Confers Resistance to
834 Venetoclax in Patients with Progressive Chronic Lymphocytic Leukemia. *Cancer Discovery* **9**, 342-
835 353, doi:10.1158/2159-8290.Cd-18-1119 (2019).
836 44 Blombery, P. *et al.* Multiple BCL2 mutations cooccurring with Gly101Val emerge in chronic
837 lymphocytic leukemia progression on venetoclax. *Blood* **135**, 773-+, doi:10.1182/blood.2019004205
838 (2020).
839 45 Tausch, E. *et al.* Venetoclax resistance and acquired BCL2 mutations in chronic lymphocytic
840 leukemia. *Haematologica* **104**, doi:ARTN e43410.3324/haematol.2019.222588 (2019).
841 46 Pan, R. *et al.* Selective BCL-2 inhibition by ABT-199 causes on-target cell death in acute myeloid
842 leukemia. *Cancer Discov* **4**, 362-375, doi:10.1158/2159-8290.CD-13-0609 (2014).
843 47 Punnoose, E. A. *et al.* Expression Profile of BCL-2, BCL-XL, and MCL-1 Predicts Pharmacological
844 Response to the BCL-2 Selective Antagonist Venetoclax in Multiple Myeloma Models. *Mol Cancer*
845 *Ther* **15**, 1132-1144, doi:10.1158/1535-7163.MCT-15-0730 (2016).
846 48 Davids, M. S. *et al.* Phase I First-in-Human Study of Venetoclax in Patients With Relapsed or
847 Refractory Non-Hodgkin Lymphoma. *J Clin Oncol* **35**, 826-833, doi:10.1200/JCO.2016.70.4320
848 (2017).
849 49 Song, T. *et al.* Bcl-2 phosphorylation confers resistance on chronic lymphocytic leukaemia cells to
850 the BH3 mimetics ABT-737, ABT-263 and ABT-199 by impeding direct binding. *Brit J Pharmacol*
851 **173**, 471-483, doi:10.1111/bph.13370 (2016).
852 50 Villalobos-Ortiz, M., Ryan, J., Mashaka, T. N., Opferman, J. T. & Letai, A. BH3 profiling discriminates
853 on-target small molecule BH3 mimetics from putative mimetics. *Cell Death Differ* **27**, 999-1007,
854 doi:10.1038/s41418-019-0391-9 (2020).

855 51 Ryan, J., Montero, J., Rocco, J. & Letai, A. iBH3: simple, fixable BH3 profiling to determine apoptotic
856 priming in primary tissue by flow cytometry. *Biol Chem* **397**, 671-678, doi:10.1515/hsz-2016-0107
857 (2016).
858 52 Bhatt, S. *et al.* Reduced Mitochondrial Apoptotic Priming Drives Resistance to BH3 Mimetics in
859 Acute Myeloid Leukemia. *Cancer Cell* **38**, 872-890 e876, doi:10.1016/j.ccell.2020.10.010 (2020).
860 53 Ha, T. *et al.* Single-molecule fluorescence spectroscopy of enzyme conformational dynamics and
861 cleavage mechanism. *Proc Natl Acad Sci U S A* **96**, 893-898, doi:10.1073/pnas.96.3.893 (1999).
862 54 Jain, A. *et al.* Probing cellular protein complexes using single-molecule pull-down. *Nature* **473**, 484-
863 U322, doi:10.1038/nature10016 (2011).
864 55 Lee, H. W. *et al.* Real-time single-molecule coimmunoprecipitation of weak protein-protein
865 interactions. *Nat Protoc* **8**, 2045-2060, doi:10.1038/nprot.2013.116 (2013).
866 56 Lee, H. W. *et al.* Real-time single-molecule co-immunoprecipitation analyses reveal cancer-specific
867 Ras signalling dynamics. *Nat Commun* **4**, 1505, doi:10.1038/ncomms2507 (2013).
868 57 Lee, H. W. *et al.* Profiling of protein-protein interactions via single-molecule techniques predicts the
869 dependence of cancers on growth-factor receptors. *Nat Biomed Eng* **2**, 239-253,
870 doi:10.1038/s41551-018-0212-3 (2018).
871 58 Choi, B. *et al.* Single-molecule functional anatomy of endogenous HER2-HER3 heterodimers. *Elife*
872 **9**, doi:ARTN e5393410.7554/eLife.53934 (2020).
873 59 Dengler, M. A. *et al.* BAX Activation: Mutations Near Its Proposed Non-canonical BH3 Binding Site
874 Reveal Allosteric Changes Controlling Mitochondrial Association. *Cell Rep* **27**, 359-373 e356,
875 doi:10.1016/j.celrep.2019.03.040 (2019).
876 60 Peyerl, F. W. *et al.* Elucidation of some Bax conformational changes through crystallization of an
877 antibody-peptide complex. *Cell Death Differ* **14**, 447-452, doi:10.1038/sj.cdd.4402025 (2007).
878 61 Zhang, Z. *et al.* Bax forms an oligomer via separate, yet interdependent, surfaces. *J Biol Chem* **285**,
879 17614-17627, doi:10.1074/jbc.M110.113456 (2010).
880 62 Antonsson, A. & Persson, J. L. Induction of apoptosis by staurosporine involves the inhibition of
881 expression of the major cell cycle proteins at the G(2)/m checkpoint accompanied by alterations in
882 Erk and Akt kinase activities. *Anticancer Res* **29**, 2893-2898 (2009).
883 63 Pagliari, L. J. *et al.* The multidomain proapoptotic molecules Bax and Bak are directly activated by
884 heat. *Proc Natl Acad Sci U S A* **102**, 17975-17980, doi:10.1073/pnas.0506712102 (2005).
885 64 Dewson, G. *et al.* Bak activation for apoptosis involves oligomerization of dimers via their alpha6
886 helices. *Mol Cell* **36**, 696-703, doi:10.1016/j.molcel.2009.11.008 (2009).
887 65 Yoo, J., Lee, T. S., Choi, B., Shon, M. J. & Yoon, T. Y. Observing Extremely Weak Protein-Protein
888 Interactions with Conventional Single-Molecule Fluorescence Microscopy. *J Am Chem Soc* **138**,
889 14238-14241, doi:10.1021/jacs.6b09542 (2016).
890 66 Srivastava, A. K. *et al.* BAX-BAK heterodimer as a pharmacodynamic biomarker of on-target drug
891 action of Mcl-1 inhibitors to evaluate in-vivo effectiveness. *J Clin Oncol* **36**, doi:DOI
892 10.1200/JCO.2018.36.15_suppl.2582 (2018).
893 67 Zhou, L. Y. & Chang, D. C. Dynamics and structure of the Bax-Bak complex responsible for
894 releasing mitochondrial proteins during apoptosis. *J Cell Sci* **121**, 2186-2196,
895 doi:10.1242/jcs.024703 (2008).

896 68 Willis, S. N. *et al.* Apoptosis initiated when BH3 ligands engage multiple Bcl-2 homologs, not Bax or
897 Bak. *Science* **315**, 856-859, doi:10.1126/science.1133289 (2007).
898 69 Anderson, M. A. *et al.* The BCL2 selective inhibitor venetoclax induces rapid onset apoptosis of CLL
899 cells in patients via a TP53-independent mechanism. *Blood* **127**, 3215-3224, doi:10.1182/blood-
900 2016-01-688796 (2016).
901 70 Chen, H. C. *et al.* An interconnected hierarchical model of cell death regulation by the BCL-2 family.
902 *Nat Cell Biol* **17**, 1270-1281, doi:10.1038/ncb3236 (2015).
903 71 Tron, A. E. *et al.* Discovery of Mcl-1-specific inhibitor AZD5991 and preclinical activity in multiple
904 myeloma and acute myeloid leukemia. *Nat Commun* **9**, 5341, doi:10.1038/s41467-018-07551-w
905 (2018).
906 72 Matulis, S. M. *et al.* Functional profiling of venetoclax sensitivity can predict clinical response in
907 multiple myeloma. *Leukemia* **33**, 1291-1296, doi:10.1038/s41375-018-0374-8 (2019).
908 73 Gupta, V. A. *et al.* Venetoclax ex vivo functional profiling predicts improved progression-free survival.
909 *Blood Cancer J* **12**, 115, doi:10.1038/s41408-022-00710-9 (2022).
910 74 Fraser, C., Ryan, J. & Sarosiek, K. BH3 Profiling: A Functional Assay to Measure Apoptotic Priming
911 and Dependencies. *Methods Mol Biol* **1877**, 61-76, doi:10.1007/978-1-4939-8861-7_4 (2019).
912 75 Del Gaizo Moore, V. & Letai, A. BH3 profiling--measuring integrated function of the mitochondrial
913 apoptotic pathway to predict cell fate decisions. *Cancer Lett* **332**, 202-205,
914 doi:10.1016/j.canlet.2011.12.021 (2013).
915 76 Seyfried, F. *et al.* Prediction of venetoclax activity in precursor B-ALL by functional assessment of
916 apoptosis signaling. *Cell Death Dis* **10**, 571, doi:10.1038/s41419-019-1801-0 (2019).
917 77 Dohner, H. *et al.* Diagnosis and management of AML in adults: 2017 ELN recommendations from an
918 international expert panel. *Blood* **129**, 424-447, doi:10.1182/blood-2016-08-733196 (2017).
919 78 Roberts, A. W. *et al.* Efficacy of venetoclax in relapsed chronic lymphocytic leukemia is influenced by
920 disease and response variables. *Blood* **134**, 111-122, doi:10.1182/blood.2018882555 (2019).
921 79 Mato, A. R. *et al.* Real-world outcomes and management strategies for venetoclax-treated chronic
922 lymphocytic leukemia patients in he United States. *Haematologica* **103**, 1511-1517,
923 doi:10.3324/haematol.2018.193615 (2018).
924 80 Liu, Z. *et al.* Direct Activation of Bax Protein for Cancer Therapy. *Med Res Rev* **36**, 313-341,
925 doi:10.1002/med.21379 (2016).
926 81 Walensky, L. D. Targeting BAX to drug death directly. *Nat Chem Biol* **15**, 657-665,
927 doi:10.1038/s41589-019-0306-6 (2019).
928 82 Liu, Q. *et al.* Bim escapes displacement by BH3-mimetic anti-cancer drugs by double-bolt locking
929 both Bcl-XL and Bcl-2. *Elife* **8**, doi:10.7554/eLife.37689 (2019).
930 83 Bogner, C. *et al.* Allosteric Regulation of BH3 Proteins in Bcl-x(L) Complexes Enables Switch-like
931 Activation of Bax. *Mol Cell* **77**, 901-912 e909, doi:10.1016/j.molcel.2019.12.025 (2020).
932 84 Alfaro, J. A. *et al.* The emerging landscape of single-molecule protein sequencing technologies. *Nat*
933 *Methods* **18**, 604-617, doi:10.1038/s41592-021-01143-1 (2021).
934 85 Smith, M. L. & Tahir, S. K. Quantification of BCL-2 Family Members by Flow Cytometry. *Methods*
935 *Mol Biol* **1877**, 163-172, doi:10.1007/978-1-4939-8861-7_11 (2019).

936

**Acknowledgements**

We thank Shi Ho Kim and Jason Sang Hyun Park for critical reading of the manuscript, and Changwon Kim, Gee Sung Eun, and Tae Gyun Kim for active discussion concerning data analysis. This work was supported by the National Grants for Leading Scientists (NRF-2021R1A3B1071354 to T.-Y.Y.) and the Bio Medical Technology Development Program (NRF-2018M3A9E2023523 to T.-Y.Y.) funded by the National Research Foundation of South Korea. This work was also supported by the Korea Health Technology R&D Project of the Korea Health Industry Development Institute (KHIDI) (HI14C1277 to Y.K.) funded by the Ministry of Health & Welfare of South Korea.

**Author contributions**

T.-Y.Y. conceived of and supervised the project. C.C., J.M.B., M.C., H.L., B.C., Y.K., and T.-Y.Y. designed the experiments. C.C. and M.C. performed the single-molecule pull-down and co-IP experiments. C.C. and H.K. measured the inter-chip CVs of the immunoassays. J.M.B. and Y.K. collected and characterized primary AML samples and performed *in vivo* ABT-199 treatment journey. C.C., Y.L., and H.P. developed the PPI probes for PBA. C.C., M.C., B.C., H.K., S.H., and Y.L. performed the PPI profiling for the primary AML samples. C.C. and Y.L. performed BH3 profiling for the primary AML samples. C.C. and S.H. performed flow cytometry for the primary AML samples. C.C. and M.C. measured the *ex vivo* drug efficacies of the primary AML samples. H.L. developed the *ex vivo* drug efficacy predicting programs. C.C. analyzed and visualized all data. C.C. and T.-Y.Y. wrote the manuscript with inputs from all authors.

**Competing interests**

C.C., M.C., H.L., B.C., S.H., Y.L., Y.K., and T.-Y.Y. filed a patent on these findings (10-2020-0157961).

963 ## Figures and figure legends

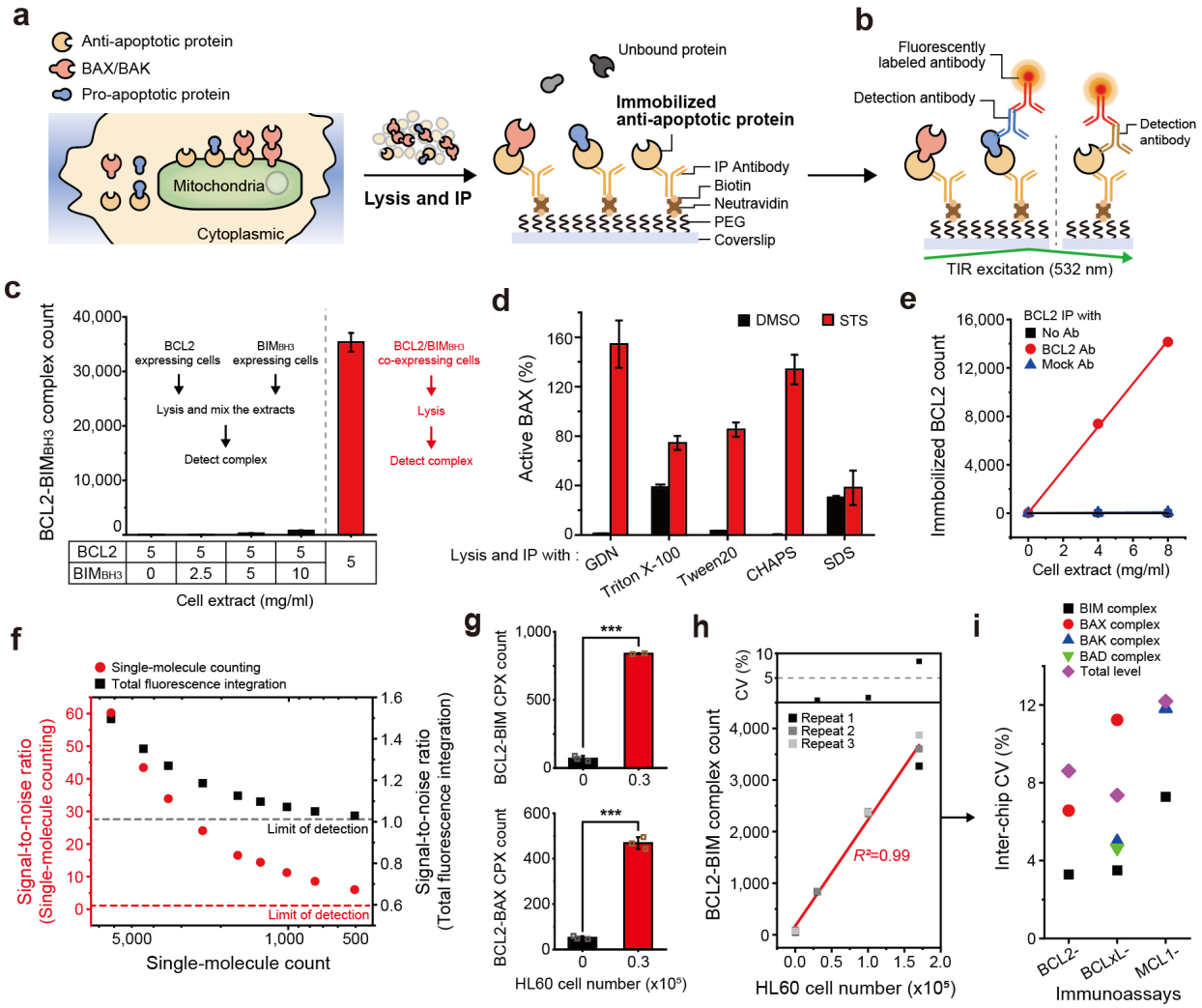


964

965 **Fig. 1 | Profiling BCL2 family protein complexes using the SMPC platform. a**, Schematic for the surface
966 IP of BCL2 family proteins. Anti-apoptotic proteins (BCL2, BCLxL, MCL1) in crude cell extracts were
967 immobilized onto the surface of the reaction chamber. **b**, Schematic of immunoassay selectively detecting
968 protein complexes (left) and the total level of surface bait protein (right). The fluorescence signals from
969 detection antibodies were imaged under total internal reflection (TIR) excitation. **c**, Comparing the formation
970 of model BCL2-BIM$_{BH3}$ complex in an intracellular environment by BCL2-mCherry/BIM$_{BH3}$-eGFP co-
971 transfection (red) and *in vitro* mixing of two individual extracts with each expressing BCL2-mCherry and
972 BIM$_{BH3}$-eGFP (black). **d**, Relative changes of active BAX level measured for STS treated HL60 cells after
973 lysed with different detergent types. The monoclonal antibody 6A7 was used to detect the activated BAX[60].
974 **e**, Surface-immobilization of BCL2-eGFP from the crude extract with indicated IP antibodies. **f**, Comparison
975 of signal-to-noise ratio between single-molecule counting analysis (red) and integration of total fluorescence
976 signals (black). **g**, Counts of endogenous BCL2 protein complexes (BCL2-BIM, BCL2-BAX) from the 30,000
977 HL60 cells by using immunoassay. Error bars represent mean±s.d from independent inter-chip
978 measurement ($n$=3). (Two-sided two-sample $t$-test, $p$-value=1.5e-5, 1.1e-5 respectively). **h**, Counts of
979 endogenous BCL2-BIM complexes and inter-chip CVs from the fixed numbers of HL60 cells ($n$=3). **i**, Inter-
980 chip CVs obtained from independent inter-chip measurement for all the immunoassays and cell numbers
981 ($n$=3). Error bars represent means±s.d.
982

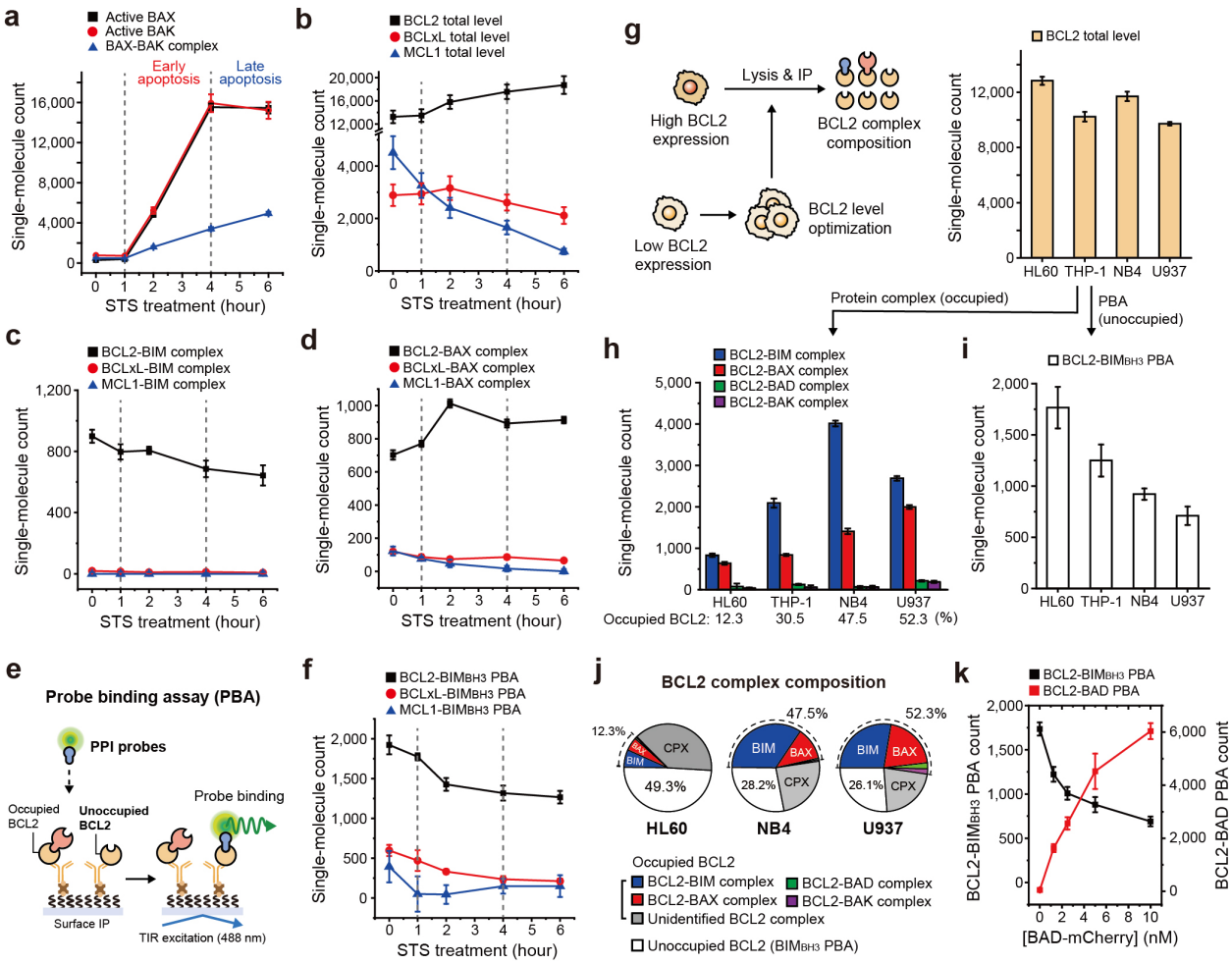


**Fig. 2 | Tracking the responses to intrinsic apoptotic stress with SMPC. a-d**, Changes of endogenous BCL2 family PPI profiles of HL60 cells through the apoptosis progression by 2 μM of STS. (**a**) Active BAX/BAK level, (**b**) Total levels of anti-apoptotic proteins (BCL2, BCLxL, MCL1), (**c**) BIM complexes with anti-apoptotic proteins, (**d**) BAX complexes with anti-apoptotic proteins. **e**, Schematic for the probe binding assay (PBA) to measure the unoccupied populations of surface-immobilized anti-apoptotic proteins. **f**, Changes of $BIM_{BH3}$ PBAs for anti-apoptotic proteins from HL60 cells through the apoptosis progression by STS. **g**, Schematic for the comparison of the BCL2 protein complex compositions in different AML cell lines. The density of surface-immobilized BCL2 was constantly maintained by optimizing the total protein concentration of crude cell extracts for all AML cell lines (HL60, THP-1, NB4, U937). **h**, Compositions of the BCL2 complexes (BIM, BAX, BAD, BAK) in four different AML cell lines. **i**, BCL2-$BIM_{BH3}$ PBA counts of four AML cell lines. **j**, The BCL2 complex compositions in HL60, NB4, and U937 cell extracts. **k**, Changes of BCL2-$BIM_{BH3}$ PBA and BCL2-BAD PBA with increasing amounts of BAD probe. $BIM_{BH3}$ probe was presented in 10 nM. Error bars represent means±s.d. The single-molecule counts were rescaled to account for the labeling efficiencies of the immunoassays (Extended Data Fig. 5) as well as the specific incubation conditions.

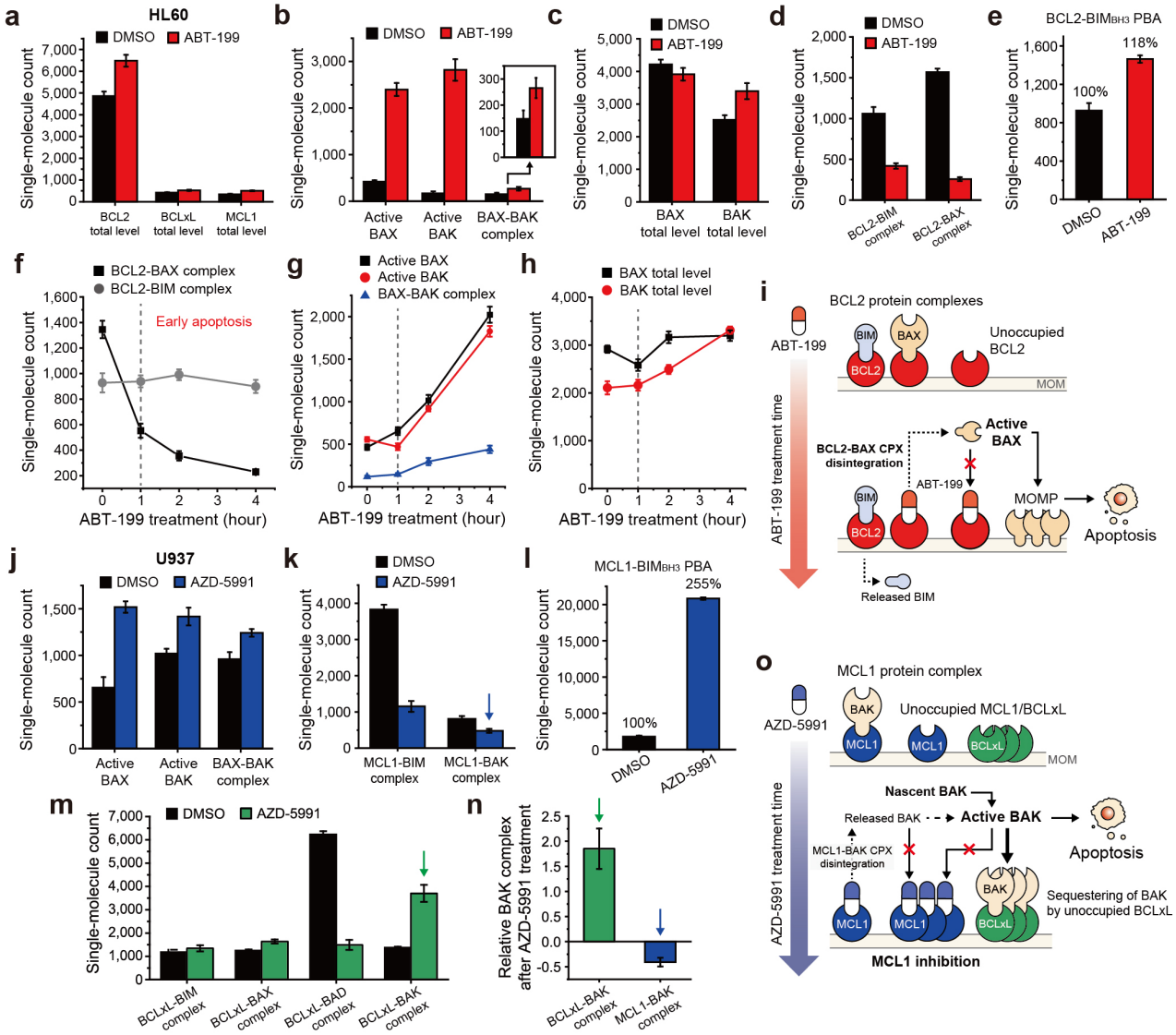


**Fig. 3 | Changes in the BCL2 family protein complexes provoked by BH3 mimetics. a-e**, Changes of BCL2 family PPI profile in HL60 cells after ABT-199 treatment (100 nM, 24 hours). (**a**) Total levels of anti-apoptotic proteins, (**b**) Active BAX/BAK level, (**c**) Total levels of BAX/BAK, (**d**) BCL2 complexes (BIM, BAX), (**e**) BCL2-BIM$_{BH3}$ PBA. **f-h**, Changes of BCL2 family PPI profile in HL60 cells after higher concentration of ABT-199 treatment (300 nM, 4 hours). (**f**) BCL2 complexes (BIM, BAX), (**g**) Active BAX/BAK level, (**h**) Total levels of BAX/BAK. **i**, Schematic illustration of the mode of action of ABT-199. **j-l**, Changes of BCL2 family PPI profile in U937 cells after AZD-5991 treatment (100 nM, 24 hours). (**j**) Active BAX/BAK level, (**k**) MCL1 complexes (BIM, BAK), (**l**) MCL1-BIM$_{BH3}$ PBA. The decrease of MCL1-BAK complex after AZD-5991 treatment was indicated (blue). **m**, Changes of BCLxL complexes (BIM, BAX, BAD, BAK) from U937 cells after AZD-5991 (100 nM, 24 hours) treatment. The increase of BCLxL-BAK complex after AZD-5991 treatment was indicated (green). **n**, Comparison of relative changes of BAK complexes from U937 cells after AZD-5991 treatment. The relative changes were obtained from the indicated data in (**k**) and (**m**). **o**, Schematic illustration of the mode of action of AZD-5991. (**d**,**k**,**m**) The single-molecule counts were rescaled to account for the labeling efficiencies of the immunoassays. Error bars represent means±s.d.

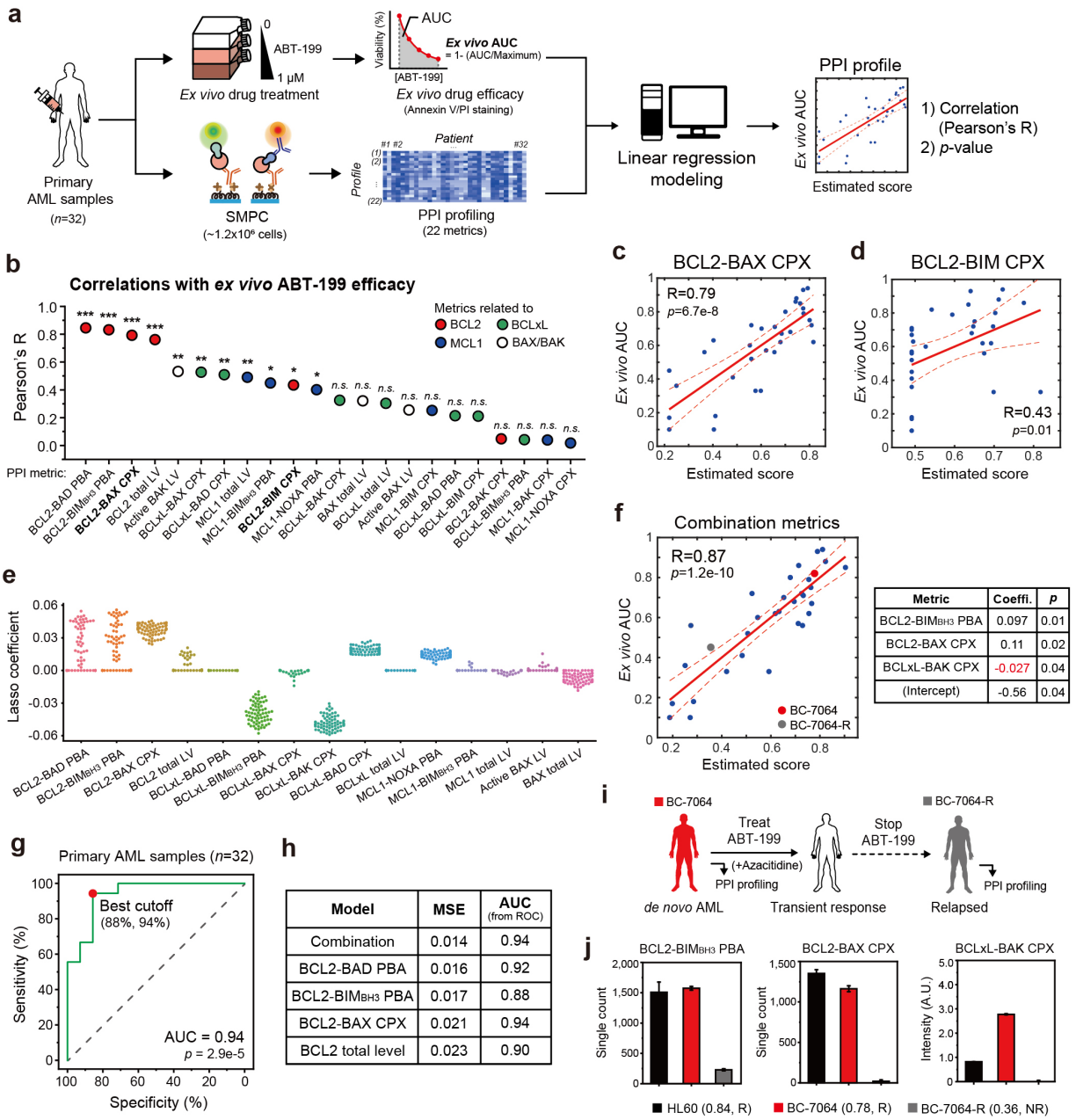


| Metric | Coeffi. | p |
|---|---|---|
| BCL2-BIMBH3 PBA | 0.097 | 0.01 |
| BCL2-BAX CPX | 0.11 | 0.02 |
| BCLxL-BAK CPX | -0.027 | 0.04 |
| (Intercept) | -0.56 | 0.04 |

| Model | MSE | AUC (from ROC) |
|---|---|---|
| Combination | 0.014 | 0.94 |
| BCL2-BAD PBA | 0.016 | 0.92 |
| BCL2-BIMBH3 PBA | 0.017 | 0.88 |
| BCL2-BAX CPX | 0.021 | 0.94 |
| BCL2 total level | 0.023 | 0.90 |

**Fig. 4 | Constructing an analysis model for ABT-199 efficacy with multi-dimensional PPI profiling. a**, Schematic for generating linear regression correlation between *ex vivo* efficacy of ABT-199 and PPI profiles from primary AML samples. The collected AML cells were cultured and treated with 0-1 μM of ABT-199, and the area under curves (AUCs) of cell viability were obtained as *ex vivo* drug efficacy (upper). ~1.2x10$^6$ of primary AML cells on the same cohort underwent PPI profiling with the SMPC platform (lower) (*n*=32). **b**, Pearson correlations between *ex vivo* AUC of ABT-199 and PPI metrics for primary AML samples (*p-value*: *<0.05, **<0.01, ***<0.001, *n.s.*=not significant). **c**,**d**, Correlations between *ex vivo* AUC and single BCL2-related PPI metrics. (**c**) BCL2-BAX CPX, (**d**) BCL2-BIM CPX. **e**, Lasso coefficients of PPI profiles correlated with *ex vivo* AUC of ABT-199 for primary AML samples (67 models). **f**, Correlation between *ex vivo* AUC and combination of multiple PPI metrics (BCL2-BIM$_{BH3}$ PBA, BCL2-BAX CPX, and BCLxL-BAK CPX). The statistical indicators (coefficient and *p*-value) of each metric were presented. **g,** Receiver operating characteristic (ROC) curve between the estimated score and the *ex vivo* efficacy. **h,** Comparison of predictive powers between analysis models. **i**, Clinical features and the ABT-199 administration history of BC-7064. **j**, Comparison of the PPI profiles and the estimated scores with PPI diagnostic results (R: responsive, NR: non-responsive) from the initial and the relapsed BC-7064 samples. Error bars represent means ± s.d.

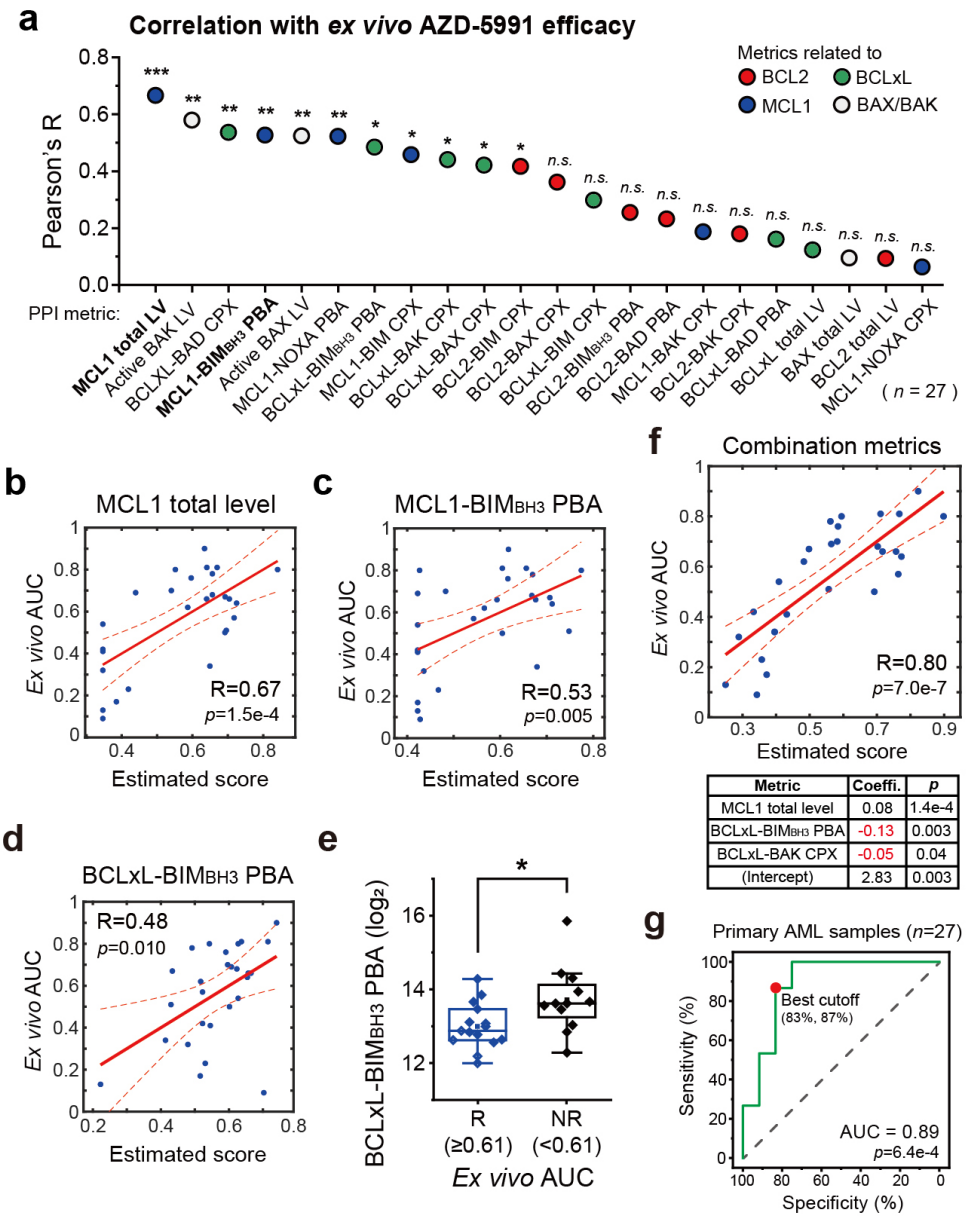


| Metric | Coeffi. | p |
|---|---|---|
| MCL1 total level | 0.08 | 1.4e-4 |
| BCLxL-BIMBH3 PBA | -0.13 | 0.003 |
| BCLxL-BAK CPX | -0.05 | 0.04 |
| (Intercept) | 2.83 | 0.003 |

**Fig. 5 | Construction of an MCL1 inhibitor efficacy model. a**, Pearson correlations between *ex vivo* AUC of AZD-5991 and PPI profiles for primary AML samples (*p-value*: *<0.05, **<0.01, ***<0.001, *n.s.*=not significant, *n*=27). **b-d**, Correlations between *ex vivo* AUC and single PPI metrics. (**b**) MCL1 total level (coefficient: 0.05), (**c**) MCL1-BIM$_{BH3}$ PBA (coefficient: 0.04), (**d**) BCLxL-BIM$_{BH3}$ PBA (coefficient: -0.13). **e**, Comparison of BCLxL-BIM$_{BH3}$ PBA counts for the AZD-5991 to responsive (*ex vivo* AUC≥0.61, *n*=12) and non-responsive (*ex vivo* AUC<0.61, *n* =15) AML samples (Two-sided two-sample *t*-test, *p*-value=0.03). **f**, Correlation between *ex vivo* AUC and combination of multiple PPI metrics (MCL1 total level, BCLxL-BIM$_{BH3}$ PBA, BCLxL-BAK CPX). The statistical indicators (coefficient and *p*-value) of each metric were presented. **g,** ROC curve between the estimated score and the *ex vivo* efficacy.

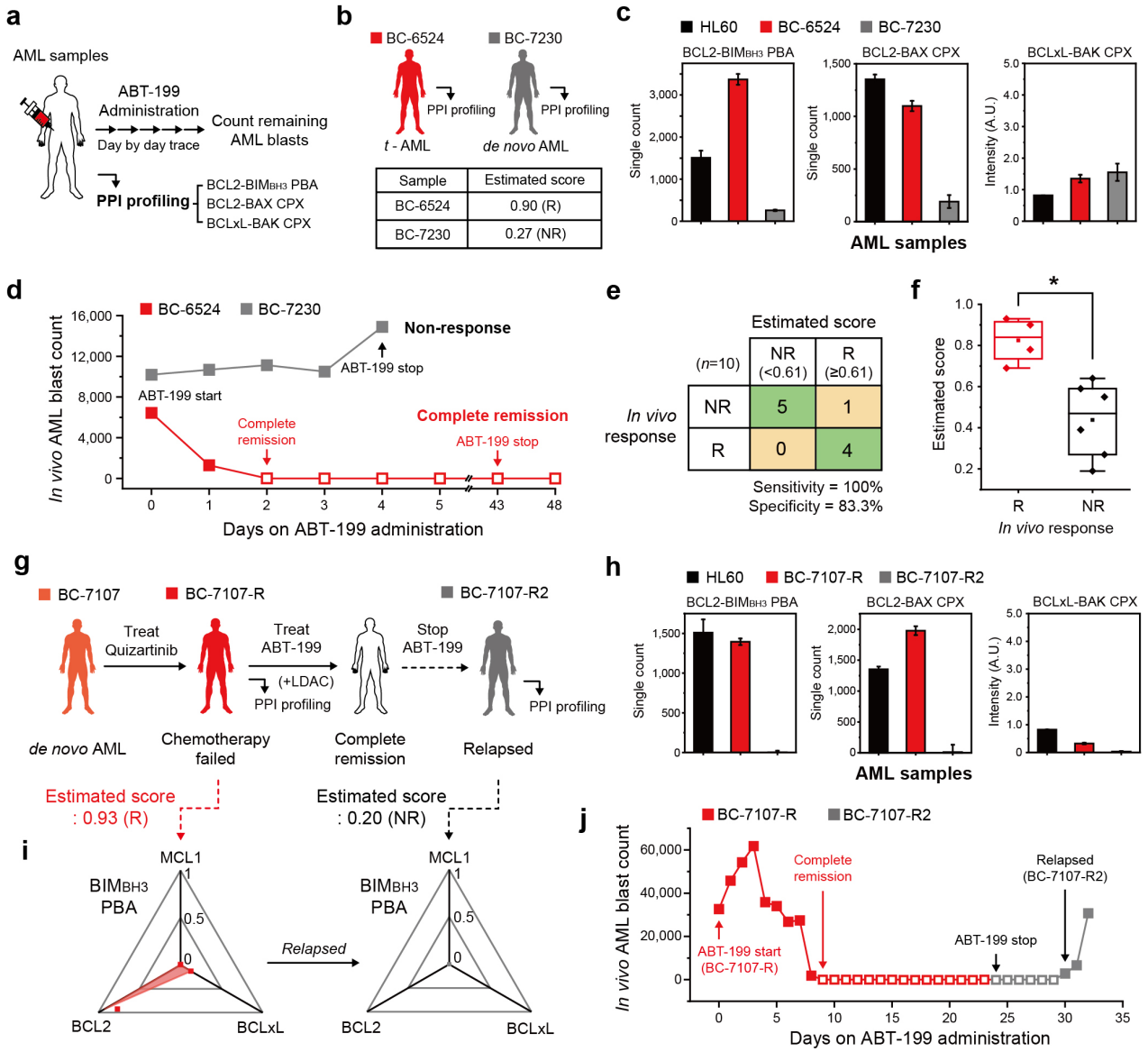


**Fig. 6 | Using the PPI analysis model as a predictive biomarker for *in vivo* ABT-199 response. a**, Schematics of the study. Complete blood cell count (CBC) analysis was carried out on a daily basis to count the number of AML blasts in the primary AML samples. **b-d**, Comparison of the PPI profiles from the BC-6524 and BC-7230 samples. (**b**) Clinical features and the estimated scores with PPI diagnostic results (R: responsive, NR: non-responsive) for ABT-199, (**c**) Comparison of BCL2 family PPI profiles, (**d**) Changes of *in vivo* AML blast counts through the days after ABT-199 administration. **e**, Confusion matrix for the drug response prediction based on the estimated score and the *in vivo* drug responses ($n$=10). **f,** Comparison of the estimated scores of AML patients between responsive ($n$=4) and non-responsive ($n$ =6) patients for *in vivo* ABT-199 administration (Two-sided Mann-Whitney test, $p$-value=0.014). **g**, Clinical features and the ABT-199 administration history of BC-7107. **h**, Tracking the changes of BCL2 family PPI profiles after relapse of BC-7107-R. **i**, Tracking the changes of $BIM_{BH3}$ PBA profiles and PPI diagnostic results after relapse of BC-7107-R. **j**, Changes of *in vivo* AML blast counts from BC-7107-R through the days after ABT-199 administration. (**b**,**g**) The estimated scores were calculated from the model in Figure 4f. Error bars represent means ± s.d.

## Extended Data Figures

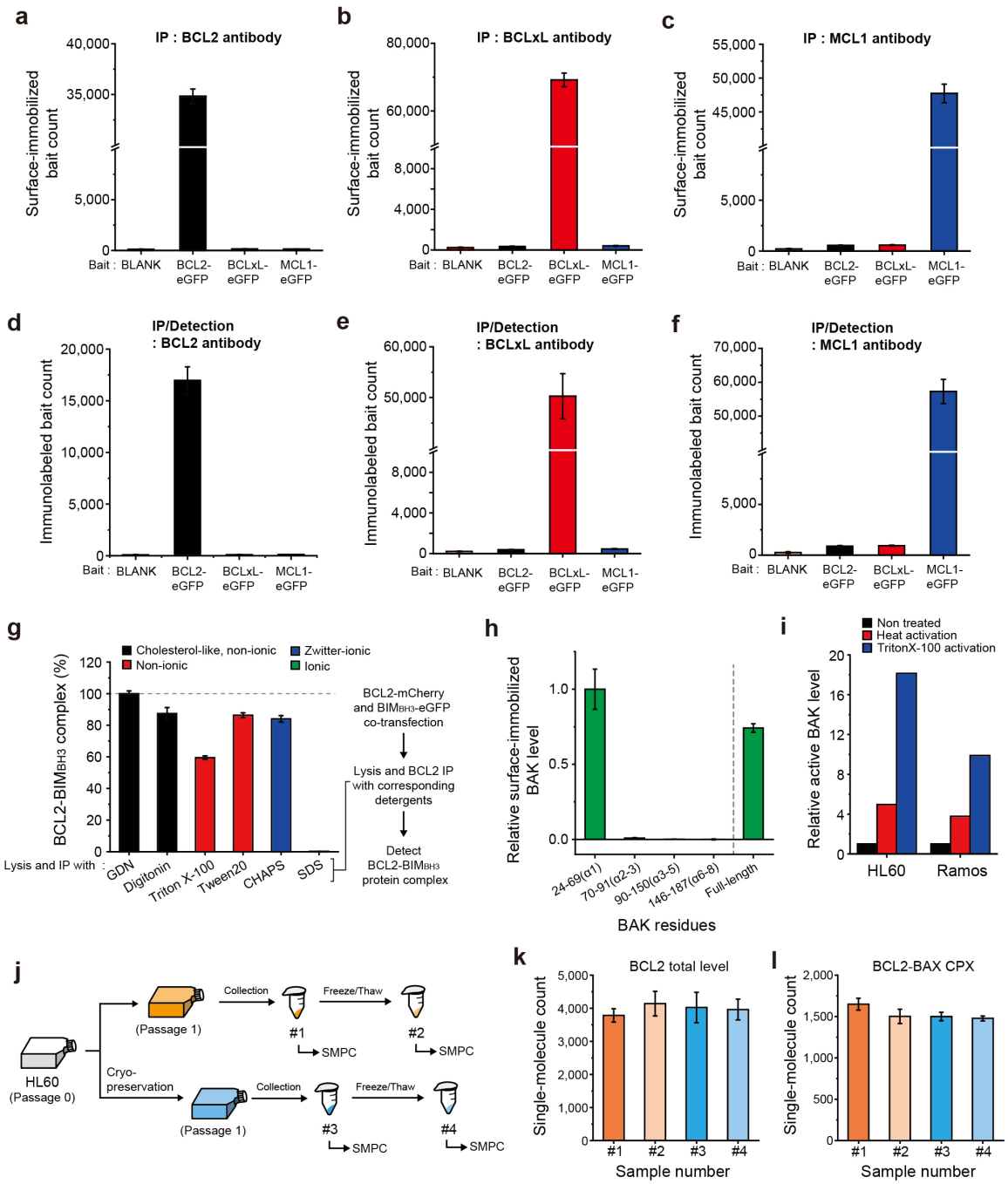


**Extended Data Fig. 1 | Development of the single-molecule pull-down and co-IP (SMPC) platform to profile BCL2 family proteins. a-c,** Selection of monoclonal antibodies for surface immunoprecipitation (IP). Surface IP of eGFP-labeled target anti-apoptotic proteins from transfected HEK293T crude cell extracts. Crude cell extracts with 1 nM of eGFP-labeled anti-apoptotic protein were used to IP. (**a**) BCL2 IP antibody, (**b**) BCLxL IP antibody, (**c**) MCL1 IP antibody. **d-f**, Selection of monoclonal antibodies for total level immunoassay of surface-immobilized target anti-apoptotic proteins. (**d**) BCL2 detection antibody, (**e**) BCLxL detection antibody, (**f**) MCL1 detection antibody. **g**, Relative model BCL2-$BIM_{BH3}$ complex from BCL2-mCherry/$BIM_{BH3}$-eGFP co-transfected HEK293T cells after the lysis with different detergent types. **h,** Detection of surface-immobilized BAK fragments by using the monoclonal antibody AT38E2. Crude cell extracts with 1 nM of eGFP-labeled BAK fragments were used to IP. **i,** Activation of BAK from HL60 and Ramos cells by heat or triton X-100 treatment to crude cell extracts[63,64]. **j,** Schematics for the preparation of HL60 samples with different preservation conditions. **k,l,** Comparison of the PPI profiles across the sample states using SMPC platform. (**k**) BCL total level, (**l**) BCL2-BAX complex. Error bars represent means±s.d.

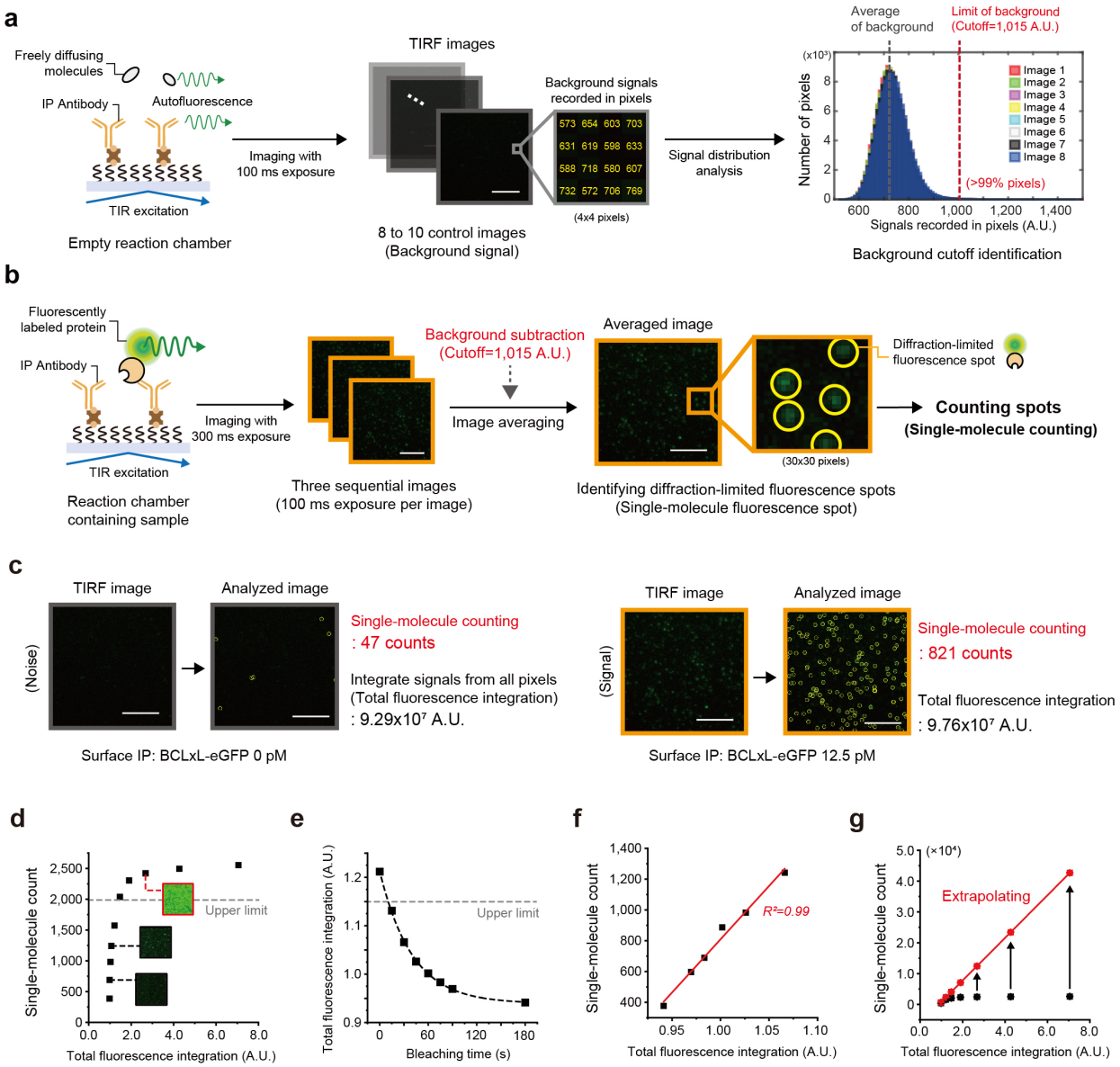


**Extended Data Fig. 2 | Post image analysis for counting the number of single-molecule fluorescence spots. a,** Setting the cutoff to eliminate background signals for post image analysis. We used 8 to 10 control images captured with a 100 ms time resolution from empty reaction chambers to establish a background limit. The background limit (cutoff=1,015 A.U.) was determined from the signal distribution recorded in each pixel of the control images, effectively eliminating 99% of background signals. **b,** Identification of diffraction-limited fluorescence spots. Three sequential images captured with a 300 ms time frame were averaged to create a single image upon subtracting the background. From the averaged image, the number of diffraction-limited fluorescence spots were counted (single-molecule counting). **c,** Identified single-molecule counts and integration of individual pixel signals of the imaging area (total fluorescence integration) from the analyzed TIRF images. (**a-d**) The TIRF images were obtained by surface IP of BCLxL-eGFP expressed in HEK293T cell extracts. (Scale bar: 10 μm). **d-g,** Calibration of single-molecule count from the total fluorescence integration. (**d**) Single-molecule count dependent on the total fluorescence integration of surface-immobilized BCL2-mCherry obtained from the analyzed images. (**e**) Photobleaching kinetics of surface-immobilized BCL2-mCherry signals depending on the bleaching time. (**f**) The linear correlation between single-molecule count and total fluorescence integration of surface-immobilized BCL2-mCherry after photobleaching. (**g**) Calibration of single-molecule count from total fluorescence integration by extrapolating. The linear correlation was obtained in (**f**). (**d-g**) The TIRF images were obtained by surface IP of BCL2-mCherry expressed in HEK293T cell extracts.

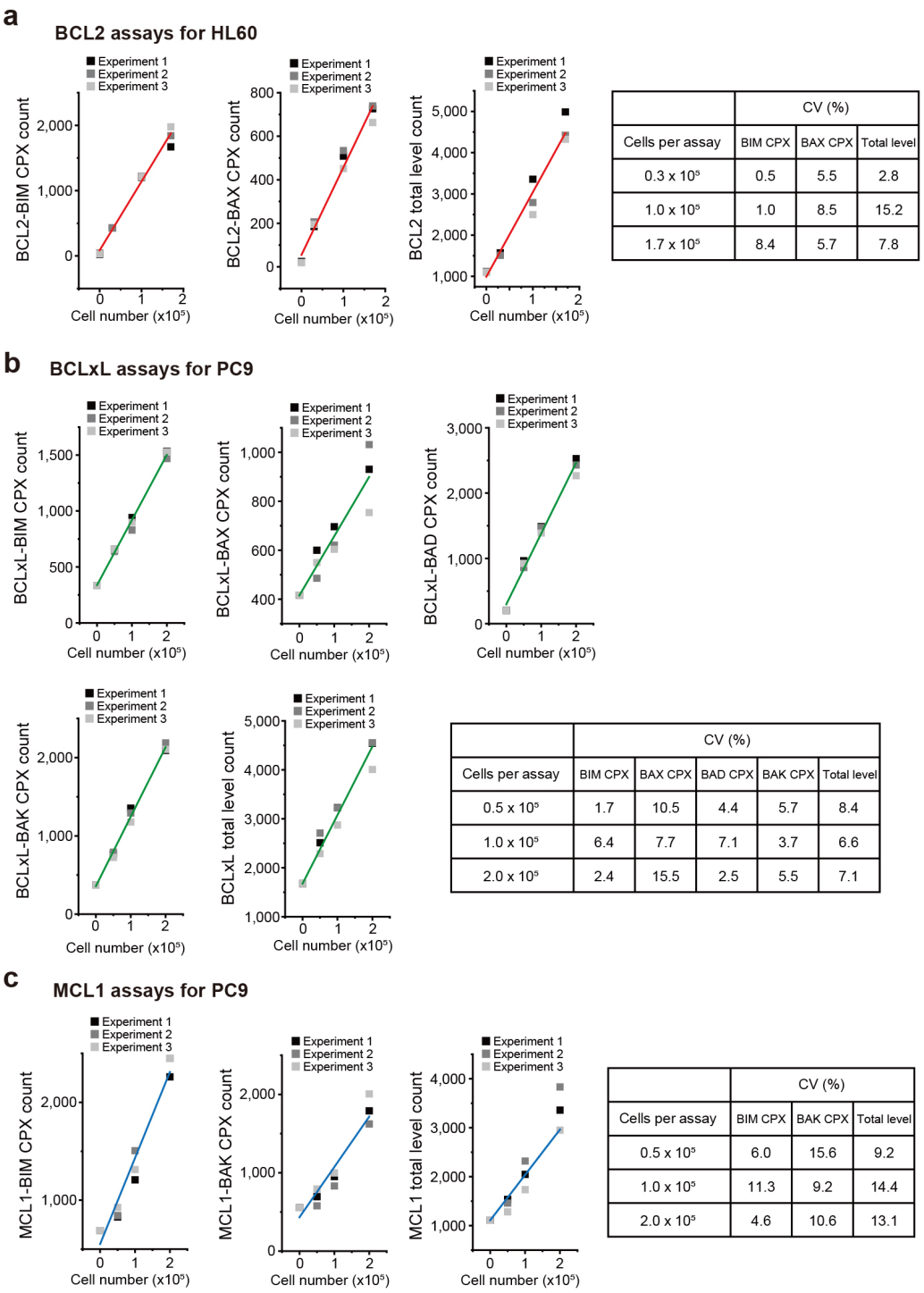


| | CV (%) | | |
|---|---|---|---|
| Cells per assay | BIM CPX | BAX CPX | Total level |
| 0.3 x 10⁵ | 0.5 | 5.5 | 2.8 |
| 1.0 x 10⁵ | 1.0 | 8.5 | 15.2 |
| 1.7 x 10⁵ | 8.4 | 5.7 | 7.8 |

| | CV (%) | | | | |
|---|---|---|---|---|---|
| Cells per assay | BIM CPX | BAX CPX | BAD CPX | BAK CPX | Total level |
| 0.5 x 10⁵ | 1.7 | 10.5 | 4.4 | 5.7 | 8.4 |
| 1.0 x 10⁵ | 6.4 | 7.7 | 7.1 | 3.7 | 6.6 |
| 2.0 x 10⁵ | 2.4 | 15.5 | 2.5 | 5.5 | 7.1 |

| | CV (%) | | |
|---|---|---|---|
| Cells per assay | BIM CPX | BAK CPX | Total level |
| 0.5 x 10⁵ | 6.0 | 15.6 | 9.2 |
| 1.0 x 10⁵ | 11.3 | 9.2 | 14.4 |
| 2.0 x 10⁵ | 4.6 | 10.6 | 13.1 |

**Extended Data Fig. 3 | Attesting the stability of the SMPC platform by inter-chip measurements of immunoassays. a**, Counts of BCL2-related immunoassays (BCL2-BIM complex, BCL2-BAX complex, BCL2 total level) from the fixed numbers of HL60 cells (*n*=3). **b**, Counts of BCLxL-related immunoassays (BCLxL-BIM complex, BCLxL-BAX complex, BCLxL-BAD complex, BCLxL-BAK complex, BCLxL total level) from the fixed numbers of PC9 cells (*n*=3). **c**, Counts of MCL1-related immunoassays (MCL1-BIM complex, MCL1-BAK complex, MCL1 total level) from the fixed numbers of PC9 cells (*n*=3). The single-molecule counts were rescaled to account for the labeling efficiencies of the immunoassays as well as the specific incubation conditions for direct comparison. All data were measured from independent inter-chip experiments. CVs obtained from independent inter-chip measurement for all the immunoassays and cell numbers (*n*=3).

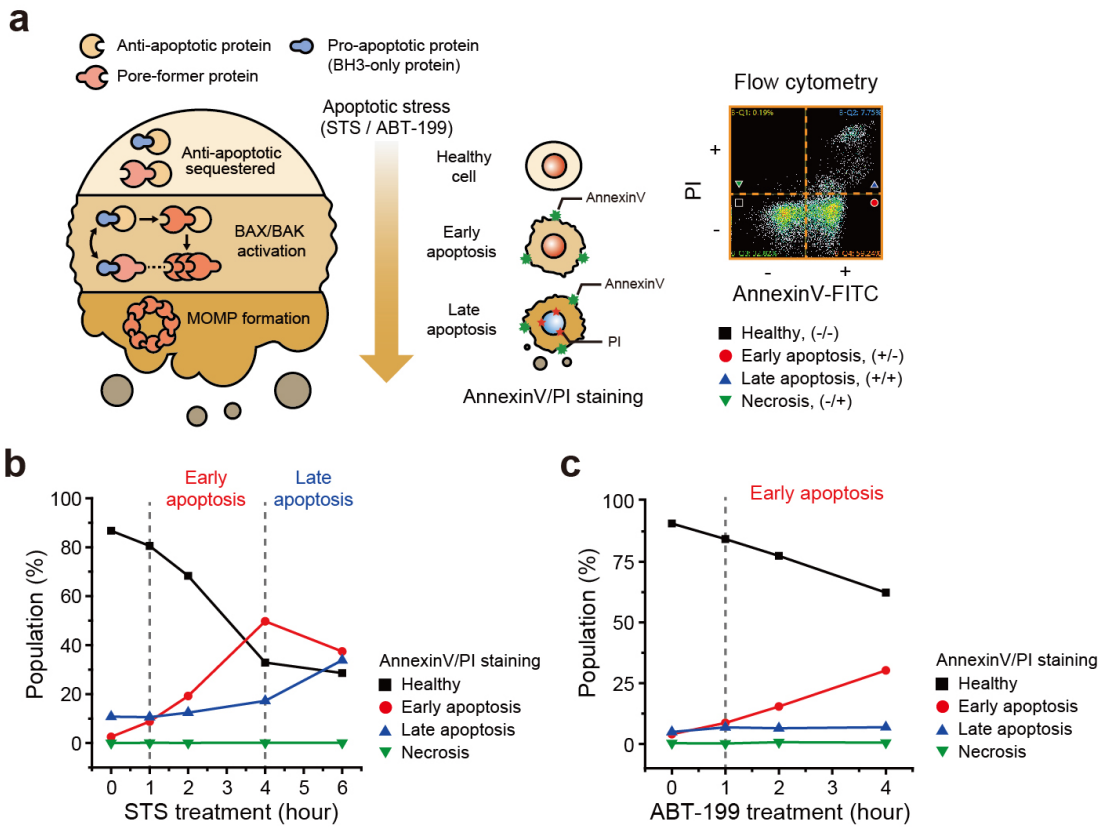


**Extended Data Fig. 4 | Tracking the response of HL60 cells under apoptotic stress. a**, Schematics for the intracellular BCL2-PPI profile changes and the result of flow cytometry analysis after Annexin V/PI staining through the progression of apoptosis pathway. **b**,**c**, Population changes of HL60 cells at different time points through the treatment of drug with Annexin V/PI staining. (**b**) 2 μM of STS, (**c**) 300 nM of ABT-199. Error bars represent means±s.d.

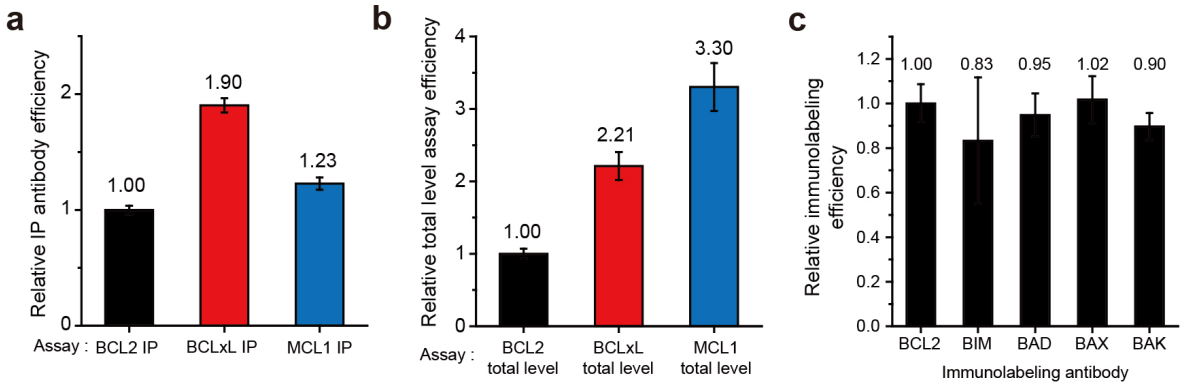


**Extended Data Fig. 5 | Relatively comparing the normalized efficiencies of different immunoassays. a**, Comparing relative efficiencies of IP antibodies for anti-apoptotic proteins. 1 nM of eGFP-labeled anti-apoptotic proteins were immobilized on the surface by the matched IP antibodies respectively, and the eGFP signals were compared. **b**, Comparing relative efficiencies of immunolabeling antibodies for anti-apoptotic proteins. The surface immobilized anti-apoptotic protein in (**a**) were immunolabeled by the matched labeling antibodies respectively, and the relative efficiencies for total level assays were compared. **c**, Comparing relative immunolabeling efficiencies of detection antibodies for BCL2 family proteins. 1 nM of eGFP-labeled BCL2 family proteins were immobilized on the surface by the anti-eGFP antibody and detected with matched detection antibodies for immunolabeling. The relative immunolabeling efficiencies of the detecting antibodies were calculated based on the ratio of labeled proteins to the total number of proteins immobilized on the surface. Error bars represent means±s.d.

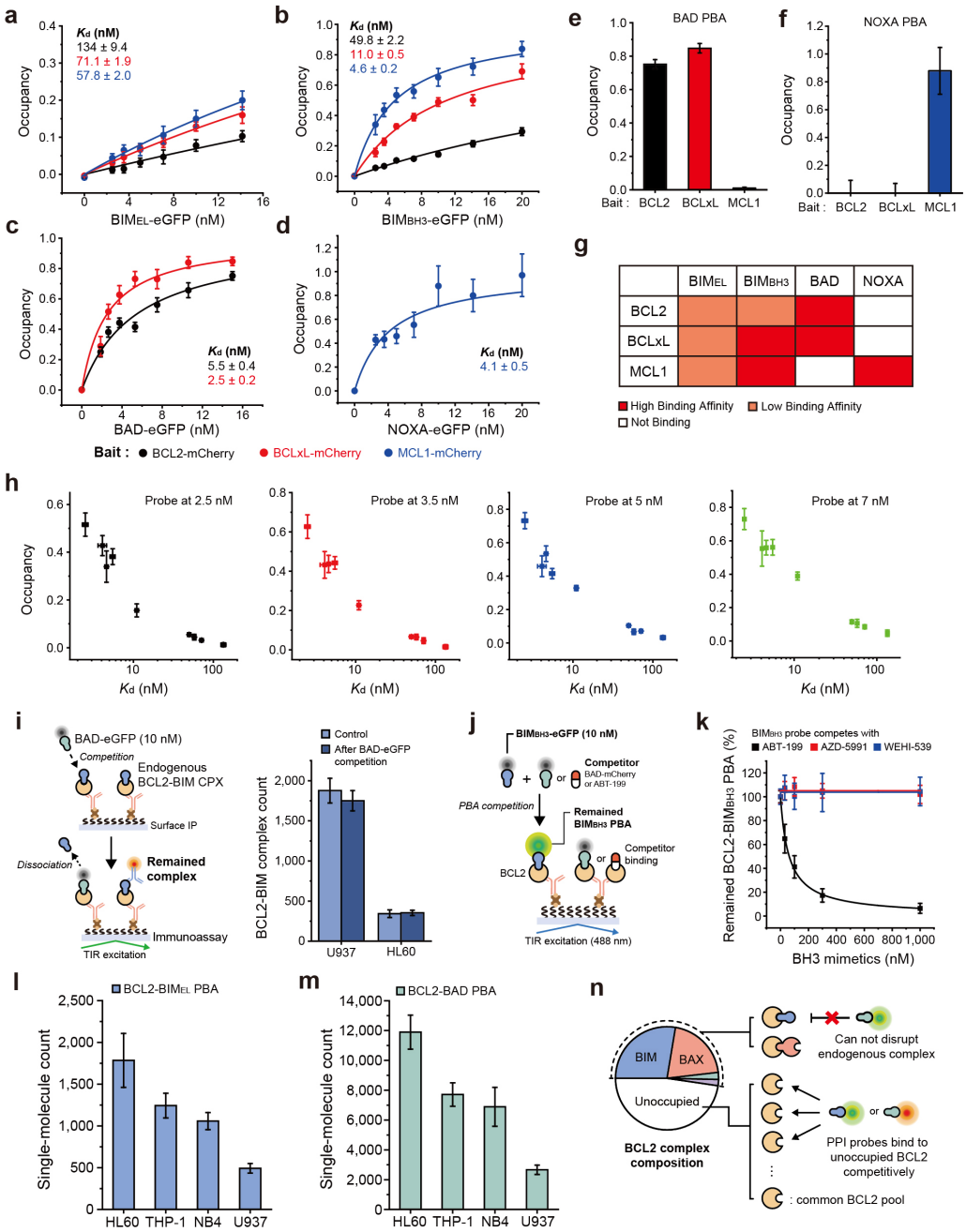


**Extended Data Fig. 6 | Population profile of PPI probes binding onto unoccupied BCL2 and the cartoon schematic of the experiment. a-d**, PBA binding curves for each PPI probes (eGFP-labeled $BIM_{EL}$, $BIM_{BH3}$, BAD, NOXA) to anti-apoptotic proteins (mCherry-labeled BCL2, BCLxL, MCL1) to calculate dissociation constant ($K_d$). (**a**) $BIM_{EL}$-PBA, (**b**) $BIM_{BH3}$-PBA, (**c**) BAD-PBA, (**d**) NOXA-PBA. **e,f,** PBA binding patterns of each PPI probe. (**e**) BAD-PBA, (**f**) NOXA-PBA. **g**, Comparison of the binding affinities between each binding pairs. **h,** Correlations between the calculated $K_d$ values and the occupancy values at a fixed PPI probe concentration. **i,** Dissociation of BCL2-BIM complex after *in vitro* competition by BAD-eGFP PPI probes. Protein complexes were surface-immobilized by anti-BCL2 IP antibody and detected with anti-BIM detection antibody after the competition (inset). **j,** Schematic of *in vitro* PBA competition between $BIM_{BH3}$-eGFP PPI probe and competitors (PPI probe or BH3 mimetics) on surface-immobilized BCL2 proteins. **k**, Remained BCL2-$BIM_{BH3}$ PBA after *in vitro* binding competition with BH3 mimetics (ABT-199, AZD-5991, WEHI-539). $BIM_{BH3}$ PPI probe was presented in 10 nM. **l,m,** BCL2 PBA counts with different PPI probes from four AML cell lines (HL60, THP-1, NB4, U937). (**l**) BCL2-$BIM_{EL}$ PBA, (**m**) BCL2-BAD PBA. **n**, Schematic for selective binding of PPI probes for unoccupied BCL2 proteins. Error bars represent means±s.d.

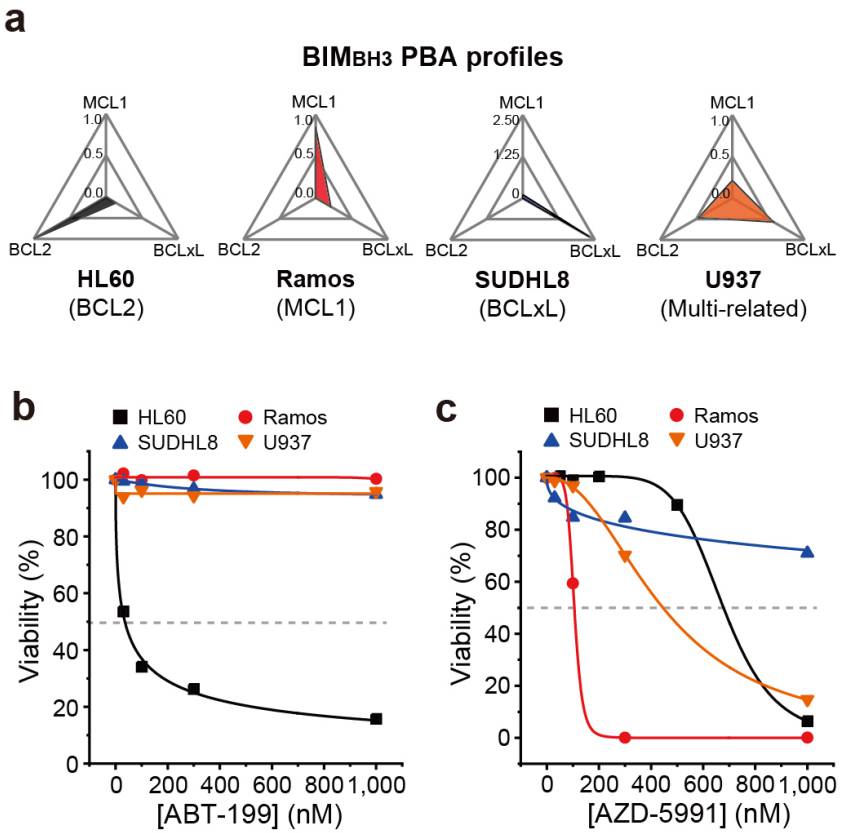


**Extended Data Fig. 7 | $BIM_{BH3}$ PBA profile predicts response of single-agent BH3 mimetics on leukemia cell lines. a**, $BIM_{BH3}$ PBA profiles of four different leukemia cell lines (HL60, Ramos, SUDHL8, U937). The $BIM_{BH3}$ PBA levels were rescaled to account for the relative binding affinities of $BIM_{BH3}$ probe for anti-apoptotic proteins determined in Extended Data Fig .6b. **b,c**, Viability of leukemia cell lines after treatment of BH3 mimetics for 24 hours. Viability represents the double negative populations after Annexin V/PI staining and analyzed with flow cytometry. (**b**) ABT-199, (**c**) AZD-5991.

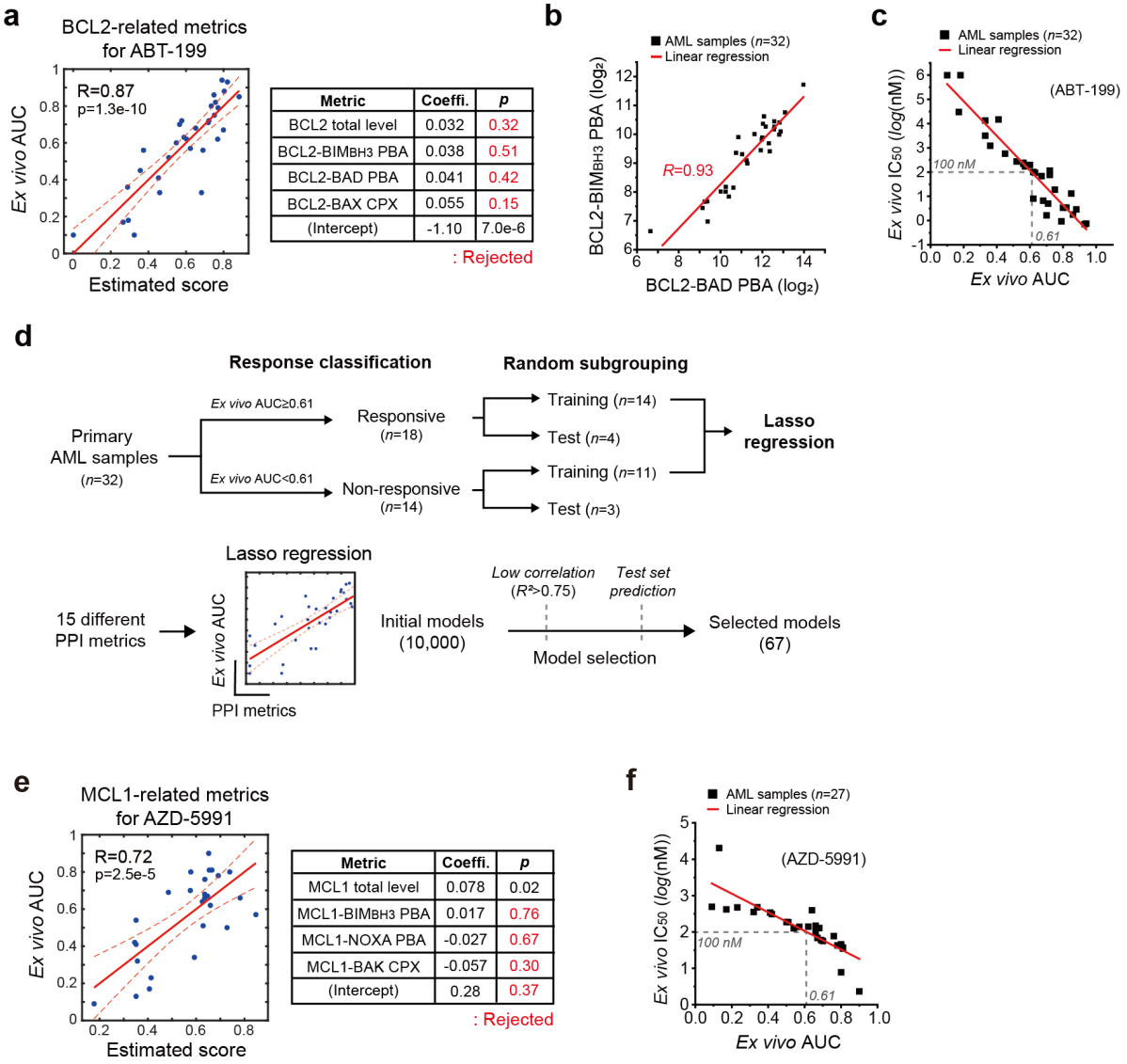


**Extended Data Fig. 8 | Development of the *ex vivo* drug efficacy prediction model with combination of multiple-PPI metrics. a**, Correlation between *ex vivo* AUC for ABT-199 and combination of BCL2-related metrics (BCL2 total level, BCL2-BIM$_{BH3}$ PBA, BCL2-BAD PBA, and BCL2-BAX CPX). **b,** Linear correlations between two different BCL2 PBA metrics. **c,** Correlations between *ex vivo* AUC and IC$_{50}$ of primary AML samples for ABT-199 (*n*=32). **d,** Schematic of Lasso regression analysis for the selection of PPI metrics highly correlated with drug response. The training and test groups were randomly selected from the primary AML sample cohort. The Lasso regression models were generated using the training group and evaluated based on Pearson's R as well as prediction outcomes for the test group. 67 models were selected from 10,000 different initial models. **e,** Correlation between *ex vivo* AUC for AZD-5991 and combination of MCL1-related metrics (MCL1 total level, MCL1-BIM$_{BH3}$ PBA, MCL1-NOXA PBA, and MCL1-BAK CPX). **f,** Correlations between *ex vivo* AUC and IC$_{50}$ of primary AML samples for AZD-5991 (*n*=27).

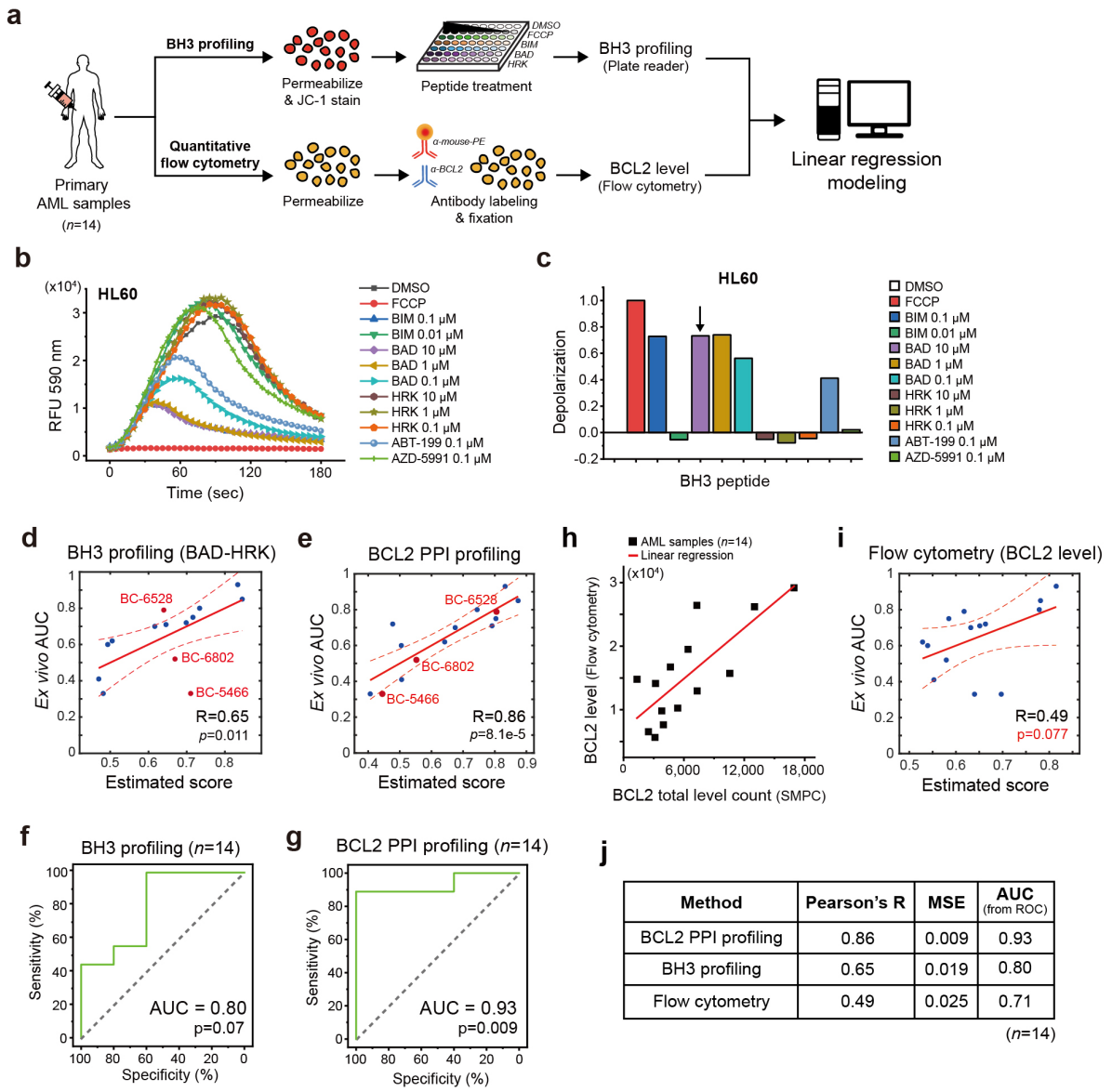


| Method | Pearson's R | MSE | AUC (from ROC) |
|---|---|---|---|
| BCL2 PPI profiling | 0.86 | 0.009 | 0.93 |
| BH3 profiling | 0.65 | 0.019 | 0.80 |
| Flow cytometry | 0.49 | 0.025 | 0.71 |

(*n*=14)

**Extended Data Fig. 9 | Comparison of BCL2 PPI profiling and different methods to predict BH3 mimetics response. a**, Schematic for BH3 profiling based on JC-1 staining (upper) and measurement of BCL2 levels using flow cytometry (lower) for primary AML samples (*n*=14). **b,c,** BH3 profiling on HL60 cells. (**b**) Relative fluorescence units (RFU) of 590 nm wavelength for HL60 cells through the treatment of BH3 peptides (BIM, BAD, and HRK) or BH3 mimetics (ABT-199 and AZD-5991). (**c**) Depolarization of HL60 cells through the BH3 profiling. Depolarization by 10 μM of BAD peptides was indicated. **d,e,** Correlations for *ex vivo* ABT-199 AUC with (**d**) depolarizations by BAD (10 μM) – HRK (10 μM) peptides, (**e**) combination of multiple PPI metrics (BCL2-BIM$_{BH3}$ PBA, BCL2-BAX CPX, and BCLxL-BAK CPX). The outliers identified in model (**d**) were indicated. **f,g,** Receiver operating characteristic (ROC) curve for *ex vivo* ABT-199 responses with (**f**) depolarizations by BAD (10 μM) – HRK (10 μM) peptides, (**g**) Combination of multiple PPI metrics. **h,** Correlations between BCL2 protein levels determined by SMPC and flow cytometry for primary AML samples (n=*14*). **i,** Prediction models for ABT-199 *ex vivo* AUC with BCL2 protein levels determined by flow cytometry. **j,** Comparison of the predictive powers for ABT-199 drug responses across different methods (*n*=14).

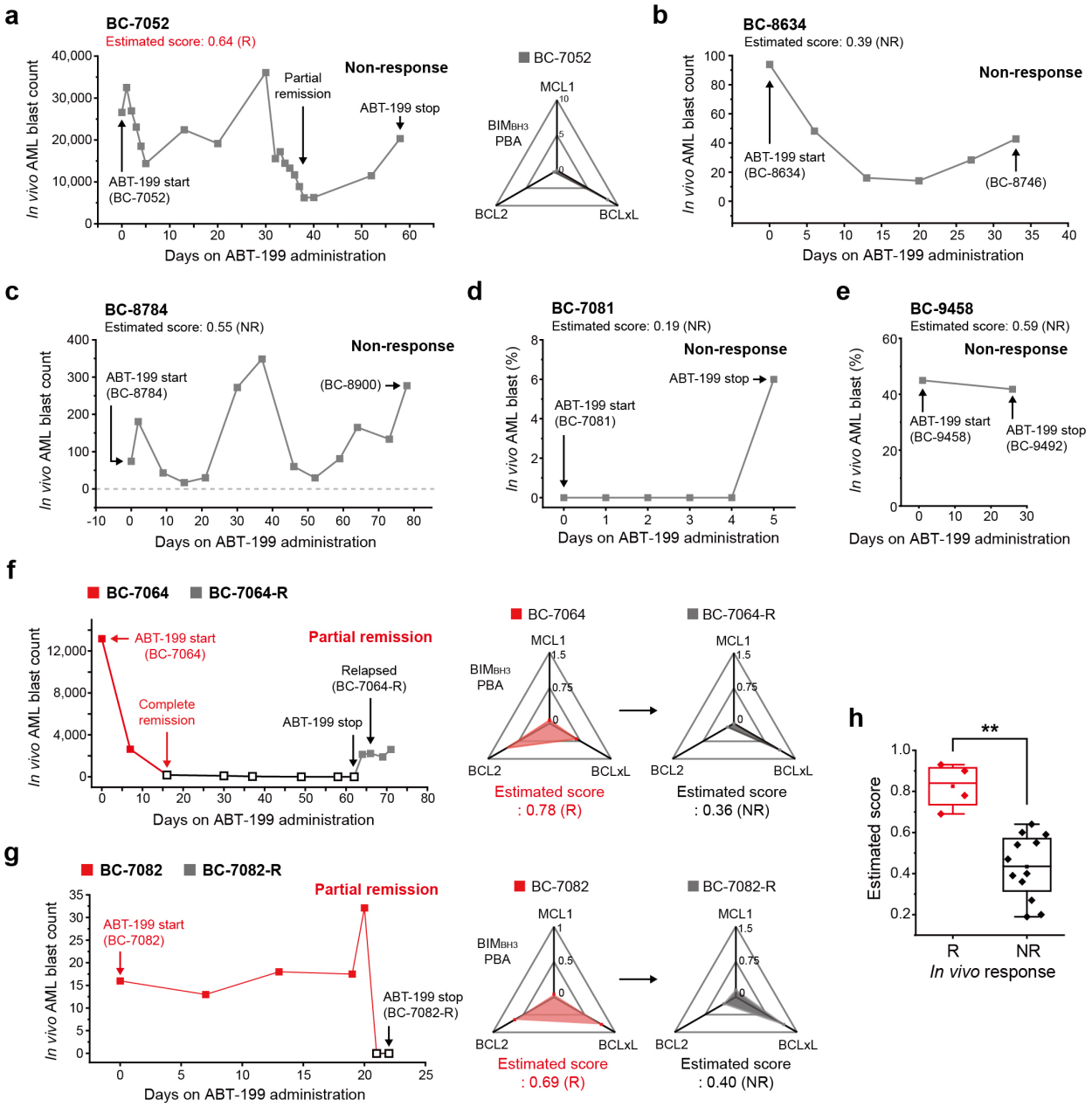


**Extended Data Fig. 10 | Longitudinal tracking of *in vivo* ABT-199 response for AML patients. a-g,** Changes of *in vivo* AML blast counts (or AML blast ratio) through the days after ABT-199 administration. (**a**) BC-7052, (**b**) BC-8634, (**c**) BC-8784, (**d**) BC-7081, (**e**) BC-9458, (**f**) BC-7064, (**g**) BC-7082. (**a-g**) The estimated scores and the PPI diagnostic results (R: Responsive, NR: Non-responsive) were obtained from the model in Figure 4f. The $BIM_{BH3}$ PBA profiles of each sample were presented. **h**, Comparison of the estimated scores of AML samples between responsive (R, *n*=4) and non-responsive (NR, *n*=10) samples for *in vivo* ABT-199 administration (Two-sided Mann-Whitney test, *p*-value=0.004). Six additional samples from the same cohort collected after relapse (BC-7064-R, BC-7082-R, BC-7107-R2, BC-8900, BC-9458, BC-9492) were included, which were categorized as the NR.